LAWRENCE
LIVERMORE
NATIONAL
LABORATORY

UCRL-JRNL-200252

Effect of stress-triaxiality on void growth in dynamic fracture of metals: a molecular dynamics study

E. T. Seppala, J. Belak, R. E. Rudd

October 13, 2003

Physical Review B

Disclaimer

Effect of stress-triaxiality on void growth in dynamic fracture of metals: a molecular dynamics study

E. T. Seppälä, J. Belak, and R. E. Rudd
Lawrence Livermore National Laboratory, Condensed Matter Physics Division, L-415, Livermore, CA 94551, USA
(Dated: October 22, 2003)

The effect of stress-triaxiality on growth of a void in a three dimensional single-crystal face-centered-cubic (FCC) lattice has been studied. Molecular dynamics (MD) simulations using an embedded-atom (EAM) potential for copper have been performed at room temperature and using strain controlling with high strain rates ranging from 10^7/sec to 10^{10}/sec. Strain-rates of these magnitudes can be studied experimentally, *e.g.* using shock waves induced by laser ablation. Void growth has been simulated in three different conditions, namely uniaxial, biaxial, and triaxial expansion. The response of the system in the three cases have been compared in terms of the void growth rate, the detailed void shape evolution, and the stress-strain behavior including the development of plastic strain. Also macroscopic observables as plastic work and porosity have been computed from the atomistic level. The stress thresholds for void growth are found to be comparable with spall strength values determined by dynamic fracture experiments. The conventional macroscopic assumption that the mean plastic strain results from the growth of the void is validated. The evolution of the system in the uniaxial case is found to exhibit four different regimes: elastic expansion; plastic yielding, when the mean stress is nearly constant, but the stress-triaxiality increases rapidly together with exponential growth of the void; saturation of the stress-triaxiality; and finally the failure.

PACS numbers: 61.72.Qq, 62.20.Mk, 62.20.Fe, 62.50.+p

I. INTRODUCTION

Ductile fracture of metals commonly occurs through the nucleation, growth and coalescence of microscopic voids.[1] Much can be learned about the ductile fracture through the study of these voids. A particularly interesting case is the dynamic fracture of ductile metals,[2–5] in which the strain rates are so high that processes such as diffusion operating on relatively long time scales may be neglected, while inertial effects become relatively important. Void growth is driven by the need to relax tensile stress that builds up in the system, and to minimize the associated elastic energy. The material around a void deforms plastically in order to accommodate the void growth. Naturally, the plastic deformation results from a local shear stress, which may arise from the applied stress, but it also may arise from the stress field of the void even if the applied stress is hydrostatic. So the expectation is that the evolution of the plastic zone, and hence the growth of the void, is influenced by the degree of stress triaxiality; *i.e.*, the ratio of the mean (hydrostatic) stress to the shear stress. It is this relationship that we study here by varying the triaxiality of the loading. In particular, we conduct simulations in which one, two or three directions of the system are expanded, producing a state of uniaxial, biaxial or triaxial strain, respectively. Variation in the triaxiality of the strain causes variation in the triaxiality of the stress state, although it should be noted that uniaxial (biaxial) strain does not imply pure uniaxial (biaxial) stress.

Besides dynamic crack propagation experiments, dynamic fracture can be measured for instance in shock physics or spallation experiments, to which the simulations performed here are compared. Various techniques are employed to generate the shock waves: Hopkinson bar, gas gun, high explosives, and laser ablation. With Hopkinson bar the strain-rates $\dot{\varepsilon}$ usually are of the order $10^2 - 10^4$/sec, in gas gun of 10^5/sec, with high-explosives even higher strain-rates can be produced, and with lasers strain-rates exceeding 10^7/sec are attained. In a gas gun for instance the fracture results from essentially one-dimensional shock loading. Two compressive shock waves are generated by the impact of a flier on a metal target, propagate away from each other, reflect from opposite free surfaces becoming tensile release waves and finally come into coincidence again. If the combined tensile stress exceeds the rupture strength of the material, the metal fails, after some incubation time, producing a fracture surface. In strong shocks, a scab of material may spall from the back side of the target and fly off. Spallation experiments[6] for single and polycrystal copper report spall strength values of $\sigma^* \simeq 3 - 4$ GPa at strain-rates $\dot{\varepsilon} \simeq 2 - 3 \times 10^5$/sec, and scaling between the spall strength and strain-rate, $\sigma^* \sim \dot{\varepsilon}^{0.2}$.

In this study of dynamic fracture in ductile metals at high strain-rates (10^7 – 10^{10}/sec) we have concentrated on void growth starting from a single crystal copper lattice containing an infinitely weakly bound inclusion or pre-existing nanoscale void. The lattice is initially free of other defects. We have focused on the effect of stress-triaxiality on void growth. In some fracture experiments, for example in necking and cup-cone fracture,[7] the triaxiality is observed to change from uniaxial to triaxial during the course of loading. It is during the triaxial phase that void growth and failure take place. Because of the connection with shock experiments, the stress triaxiality study done here is carried out using strain control, and

it is the strain that is varied from uniaxial to biaxial to triaxial.

Much of the damage modeling of metals has been carried out at mean-field or continuum level based on constitutive theories. The continuum models concentrate especially on two areas: macroscopic crack growth phenomenon[8,9] and studies of porosity, *i.e.* behavior of an array of voids, at sub-grain level during loading.[10–26] In the latter area for example the locus of yield surfaces in stress space has been studied, which is related to the question of the effect of stress-triaxiality studied here. Of the void growth studies especially the Gurson model[16] is commonly used to model cavitation at the sub-grid level. These continuum calculations often assume that the matrix material, where the voids are embedded, is elastically rigid and plastically incompressible, and the dilation of the void-matrix aggregate is completely due to the void growth. The calculations are done by determining approximate solutions for integrals of incremental equations of virtual work using the finite element method. Continuum modeling has been used to study some of the phenomena addressed in this paper such as the effect of triaxiality on void growth and void shape changes.[27] The validity of the approximate solutions of incrementals limits the strain-rates to be rather low compared to the strain-rates used in this study.

In order to characterize the void growth not only with macroscopic quantities and at the continuum level, but to investigate what happens at the atomistic level, we have employed molecular dynamics (MD) simulations. MD simulations enable us to see what the effects are on the void surface at the single atom level, when it grows while the total system yields. This Article presents work, which is an extension to the work done earlier by some of this Article's authors of void growth in a single crystal copper with hydrostatic loading, void nucleation and growth in single and polycrystalline copper.[28–33] Molecular dynamics simulations of void growth in single crystal copper have also been conducted by other groups for slab geometries of interest in the semiconductor chip metalization problem.[34,35] The effectively two-dimensional, thin film systems are in contrast to three dimensional bulk systems studied here. Also huge simulations of crack propagation (35 million atoms)[36] and of ductile failure (billion atoms)[37] have been carried out using MD.

This Article is organized as follows. It starts in Section II with an overview of the MD method used and the simulations which have been carried out in this study. Exploration of the results of the simulations starts in Section III by the study of the mean or hydrostatic stress versus strain as well as the deviatoric part of the stress tensor, Mises stress, which is used to measure the shear stress, and stress-triaxiality versus strain for all the simulated strain-rates and modes of expansion. Section IV concentrates on the macroscopic plastic quantities, such as mean and equivalent plastic strain, plastic work and its relation to the temperature. The evolution of the void in terms of its growth and shape changes is studied in Section V. Section VI summarizes the results and compares different measured quantities with each other concentrating on one of the simulations, uniaxial strain with strain-rate 10^8/sec. The Article is concluded with discussions of the results and suggestions for future studies in Section VII.

II. METHOD AND SIMULATIONS

A. Strain-controlled Molecular Dynamics

In this atomistic-level study of void growth, the simulations have been done using empirical embedded-atom (EAM) potentials in classical molecular dynamics[38] following the scheme developed earlier.[28–30] The copper EAM potential we have used is due to Oh and Johnson.[39,40]

The system, in which the simulations are done, is a three-dimensional single-crystal face-centered-cubic (FCC) lattice in a cubic box with {100} faces. Periodic boundary conditions are used in all the three directions so that there are no free boundaries in the system apart from the void. Equivalently the system can be imagined to consist of an infinite periodic array of voids. Note that periodic boundary conditions have also been used in continuum models of void growth, but in the continuum models the calculations are done in a reduced cell, which exhibits one quarter of the box in two dimensions, and one eighth in three dimensions, and the behavior of other areas are derived from the symmetries. We use the full cubic box because the cubic symmetry present in the continuum is broken in MD at finite temperature, and processes such as dislocation nucleation at the void surface would be over-constrained in a reduced simulation box.

In the simulations, the system is brought to thermal equilibrium at room temperature, $T = 300$ K, with a commonly used thermostat[41] and at ambient pressure, $P \simeq 0$ MPa, keeping the volume constant. After that a spherical void is cut in the middle of the system, later the thermostat is turned off, and the dilational strain is applied uniformly with a constant strain-rate $\dot{\varepsilon}$. The removal of the atoms in the spherical region may be considered to simulate the instantaneous separation of the matrix material from an infinitely weakly bound inclusion. The uniform expansion in these strain-controlled simulations is applied through rescaling the coordinates as in the Parrinello-Rahman method.[42] Technically the three Cartesian coordinates of the atoms are rescaled to the unit-box, each coordinate $S_\alpha \in [0, 1)$. When calculating the forces and velocities, as well as updating the new positions of the atoms, the unit-box is multiplied by a diagonal scaling matrix $\mathcal{H} = \{l_x, l_y, l_z\}$, where l's are the simulation box's side lengths, to compute the true positions of the atoms,

$$\mathbf{x} = \mathcal{H}\mathbf{S}. \tag{1}$$

This scaling matrix $\mathcal{H}$ is updated each time-step, when the load is applied, by multiplying the initial matrix $\mathcal{H}_0$ with the sum of the unit matrix and the strain matrix $\mathcal{E} = t\dot{\mathcal{E}}$,

$$\mathcal{H}(t) = \mathcal{H}_0 \cdot (\mathbb{I} + t\dot{\mathcal{E}}). \quad (2)$$

For our purposes the strain-rate matrix $\dot{\mathcal{E}}$ is always diagonal, since neither rotation nor simple shear type strains are studied. In the triaxial case all the terms in the diagonal are equal; in the uniaxial there is a single non-zero term; and in the biaxial case two of the three diagonal terms differ from zero and are equal. Prior to expansion the system is cubic, its scaling matrix $\mathcal{H}_0$ is diagonal, and all the terms are equal and correspond to the equilibrium size at ambient pressure. Hence the scaling matrix $\mathcal{H}$ remains diagonal throughout the simulation, and the strain in each case is in a $\langle 100 \rangle$ direction.

In fracture and plasticity simulations the first quantity to consider is the stress-strain behavior. With the strain as an input parameter, here we have to measure the stress. In this study of the stress-triaxiality we are interested in both mean and shear stresses. Therefore the whole stress tensor $\sigma_{\alpha\beta}$ is needed. The stress tensor (the negative of the pressure) can be calculated atomistically on each time-step using the virial formula:[38]

$$\sigma_{\alpha\beta} = -\frac{1}{V}\left(\sum_i p_{i\alpha}p_{i\beta}/m_i + \sum_i \sum_{j>i} r_{ij\alpha} f_{ij\beta}\right). \quad (3)$$

The first term in the stress tensor is the kinetic contribution of atoms denoted with i and having masses m_i and momenta p_i. The second term, a microscopic *virial* potential stress, consists of sums of interatomic forces f_{ij} of atom pairs $\langle ij \rangle$ with corresponding distances r_{ij}. It should be noted, that here and in the rest of the Article i and j denote the atoms, and α and β the Cartesian coordinates. Note that the thermal stress is included, although in practice in these simulations it contributes less than 1 GPa, less than 10% of the yield stress value, and never dominates the changes in stress.

B. Simulations Performed

Typically in the simulations carried out here, the cube consists of 60 FCC unit cells in each direction, giving 864 000 atoms. The equilibrium side-length of such a copper system is $l = 21.6$ nm at room temperature and ambient pressure. The radius of the spherical void cut from the system, unless otherwise noted, is 0.1 of the side-length of the box; thus 2.2 nm. After the void is cut, there are 860 396 atoms in the system.

The relatively inexpensive potential used enables us to do extensive simulations in time. A single time-step takes typically about 40 sec of CPU-time in a system with 864 000 atoms in a Linux workstation with Intel Xeon 1700MHz processor. The longest calculation required 835 050 time-steps corresponding to 5.6 nanoseconds. The time-step was 6.7 femtoseconds.

As mentioned earlier, in order to study the effects of the stress-triaxiality and different modes of expansion on the void-growth, we have applied three different types of expansion, namely uniaxial, biaxial, and triaxial. The strain-rates used for each of the three modes of expansion are $\dot{\varepsilon} = 10^{10}$/sec, 10^9/sec, 5×10^8/sec, 10^8/sec, and 10^7/sec. For the lowest strain-rate, the MD code was parallelized in order to take advantage of massively parallel computers. The parallelization was done using a spatial domain-decomposition, and was shown to scale nearly linearly up to 128 processors. The parallel code was used in the case with 835 050 time-steps mentioned above, for example.

For comparison in the elastic regime, we have also performed simulations without a void in all three modes of expansion. These simulations have been used to determine the bulk, elastic stress-strain response of the EAM copper and hence the elastic constants. Without a void, the system is not so strain-rate and system size dependent, at least up to the point of failure, so the so-called "no void" simulations have been performed with a smaller system size, 45 FCC-cells in each direction (364 500 atoms) and at the single strain-rate $\dot{\varepsilon} = 10^9$/sec. A uniaxial study of the 60^3 system size, but with a smaller initial void radius of 1.1 nm, was carried out with the strain-rate $\dot{\varepsilon} = 10^8$/sec in order to study the void-size dependence. In this case the system with the void contains 863 543 atoms.

It should be mentioned, too, that all of the intermediate strain-rate simulations ($\dot{\varepsilon} = 10^8$/sec and 5×10^8/sec) expansion were not started from equilibrium conditions at $P = 0$ MPa, but from systems expanded previously at the strain-rate $\dot{\varepsilon} = 10^9$/sec. These simulations have been restarted well before yielding, when the system's behavior is rate independent, and relaxed for 2000 time-steps, or 13.4 picoseconds, without expansion before continuing the expansion at the intermediate strain rates. The energy is conserved during the relaxation in MD simulations. These restarts have been accomplished at strain values $\varepsilon = 4.12$ %, $\varepsilon = 2.06$ %, and $\varepsilon = 1.72$ % in uniaxial, biaxial, and triaxial cases, respectively.

III. STRESS-STRAIN BEHAVIOR AND STRESS-TRIAXIALITY

Let us begin to explore the results of the MD simulations by looking at the stress-strain curves. Figure 1 shows these curves for each of the modes of expansion at all the strain-rates computed. The data from "no void" cases are also plotted. The mean or hydrostatic stress,

$$\sigma_m = \frac{1}{3}\,\mathrm{Tr}\,\sigma_{\alpha\beta}, \quad (4)$$

is plotted to indicate the principal impetus for void growth. Note that the strain is the *engineering strain*,

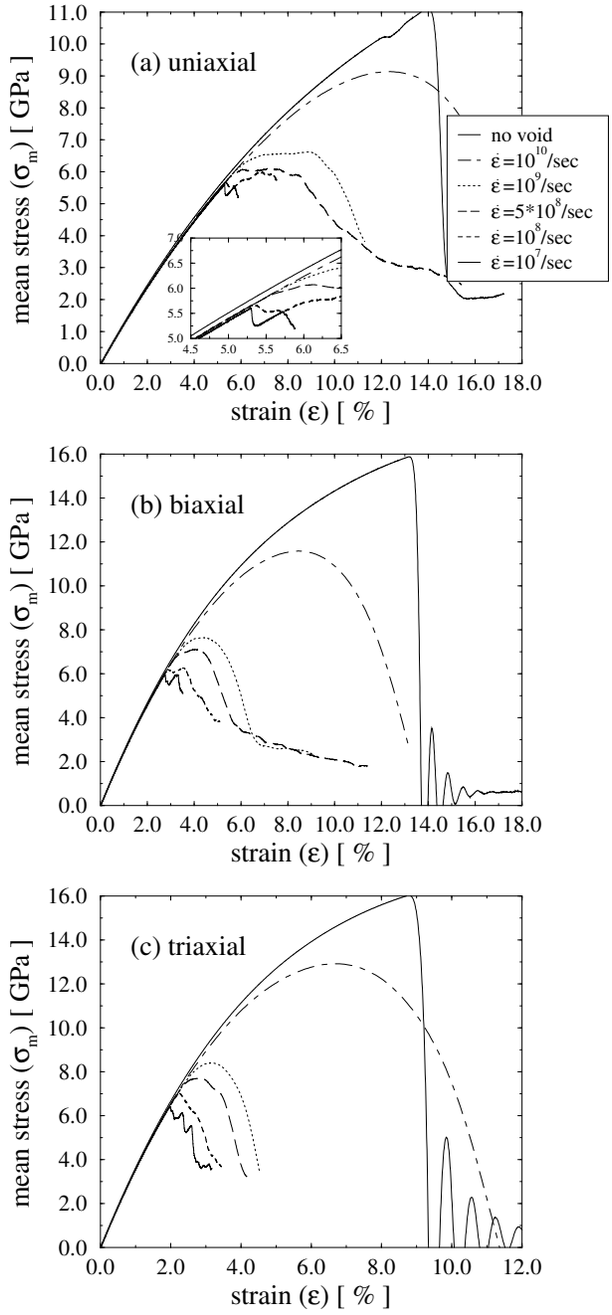

FIG. 1: Mean stress σ_m versus engineering strain ε for strain-rates $\dot{\varepsilon} = 10^{10}$/sec $(-\cdot)$, 10^9/sec $(\cdots)$, 5×10^8/sec $(--)$, 10^8/sec (- -), and 10^7/sec $(-)$. The equilibrium size of the simulation box is $[21.7\text{nm}]^3$, when $\sigma_m = 0$. The simulation box has 860 396 atoms and a pre-existing void of radius 2.2 nm. The thin solid line, drawn as a reference, is from a system with no initial void, consisting of 364 500 atoms in an equilibrium box sized $[17.5\text{nm}]^3$, and expanded at $\dot{\varepsilon} = 10^9$/sec. (a) Uniaxial expansion with $\varepsilon_x = \varepsilon$, $\varepsilon_y = \varepsilon_z = 0$. The inset zooms on the yield points of the stress-strain curve. (b) Biaxial expansion with $\varepsilon_y = \varepsilon_z = \varepsilon$, $\varepsilon_x = 0$. (c) Triaxial expansion with $\varepsilon_x = \varepsilon_y = \varepsilon_z = \varepsilon$.

defined as the expanded system size divided by the original system size minus one. In the uniaxial and biaxial cases the strains are the principal strain values in the direction of the strain, not the mean strains ε_m. Hence the strain is the value of a non-zero diagonal term of $t\dot{\mathcal{E}}$ in Eq. (2). The mean strains are 1/3 and 2/3 of the plotted uniaxial and biaxial strains, respectively. Thus the total volumetric strain-rates are not the same in the different expansion modes. In the triaxial cases the plotted and the mean strain values are the same. The shape of the stress-strain curves do not differ much depending on the modes of expansion in these cases, at least when plotted versus mean strain. Independent of the strain-rate, and whether with or without a void, the stress-strain curves lie essentially on top of each other during elastic expansion, *i.e.*, the initial smooth behavior when the system is still recoverable and has not deformed plastically.

The stress-strain curve starts to deviate from the trend of the elastic behavior at a specific, "critical" point which we call here a *yield point*. In other quantities we measure a change in behavior happens at a specific point, too, and as we shall see later the critical or yield points mostly coincide with each other, *i.e.*, their strain values are approximately the same independent of from which quantity we derived it. The same point is also the one when the void starts to grow, which is the primary mechanism for plasticity in this study. Here we define numerically the yield point of the cases with void by comparing their stress-strain curves with the reference "no void" curve, which behaves elastically beyond the yield points of the other cases [cf. Fig. 1(a) inset]. There is a small offset between cases with a void compared to the case without a void due to the elastic relaxation of the void. The value of the stress at the yield point is lower with lower strain-rate, and thus the strain to yield is also lower. In each of the modes of expansion, the stress at the yield point for the strain-rate $\dot{\varepsilon} = 10^7$/sec is close to the value to which the higher strain-rates converge. Of course, at much lower strain rates the physics changes, new mechanisms become active, so this value need not hold for arbitrarily low strain rates. However, it is noteworthy that the stress at the yield point is not scaling, contrary to the experimental finding for the spall strength explained in Section I. Overshooting, the phenomenon that the maximum stress is much higher than the stress at the yield point, is evident here for the higher strain rates. The scaling of the spall strength versus the strain-rate[6] with an exponent 0.2 is reproduced here when one compares the maximum stress values instead of the stresses at the yield point for strain-rates $\dot{\varepsilon} = 5 \times 10^8 - 10^{10}$/sec, since then the exponent is $0.14 - 0.18$, lowest for the uniaxial case and highest for the triaxial case. On the other hand the stress value at the yield point, which is at the same time the maximum stress, when $\dot{\varepsilon} = 10^7$/sec is very close to the value of 6-8 GPa the spall strength scaling predicted from the lower strain-rates mentioned in Section I. It should be noted also, that since we are limited to finite, fairly small, system sizes, at late stages of the

stress-strain curves, at the failure, the data is not realistic anymore. The reason is that at the plastic part of the stress-strain behavior when the void grows, it also emits dislocations, and in a finite system with periodic boundaries, when the dislocations have traveled long enough, they propagate through the boundaries and reenter from the other side. In the picture where we have a periodic array of voids in an infinite system this means that the voids are so close to each other that they start to interact. In reality voids are never arranged in a perfect cubic lattice structure and in symmetric positions with respect to each other, and thus the interactions of the voids in the simulations with their periodic images are just an unphysical finite size effect.

In the shear stress or more precisely in the deviatoric part of the stress tensor σ_e plotted in Fig. 2, a much bigger difference is seen between the modes of expansion than in the mean stress. For the deviatoric part of the stress σ_e we use *von Mises stress*:

$$\sigma_e = [3\, J_2]^{1/2}, \tag{5}$$

where $J_2 = \frac{1}{2}\mathrm{Tr}\ \sigma'^2$ is the second invariant of the stress deviator $\sigma'_{\alpha\beta} = \sigma_{\alpha\beta} - \sigma_m \mathbb{I}$.[43] Thus von Mises stress or simply Mises stress reads:

$$\begin{aligned} \sigma_e &= \left[3\left(\sum_{\alpha>\beta}\sigma^2_{\alpha\beta} - \sum_{\alpha>\beta}\sigma'_{\alpha\alpha}\sigma'_{\beta\beta}\right)\right]^{1/2} \\ &= \left[\tfrac{1}{2}\sum_{\alpha>\beta}(\sigma_{\alpha\alpha}-\sigma_{\beta\beta})^2 + 3\sum_{\alpha>\beta}\sigma^2_{\alpha\beta}\right]^{1/2}. \end{aligned} \tag{6}$$

While the mean stress at the yield point gets a value of about $\sigma = 5.6 - 6.4$ GPa when loaded with strain-rate $\dot{\varepsilon} = 10^7$/sec in each of the three modes of expansion, the Mises stress has a value of $\sigma_e = 2.0$ GPa and 0.7 GPa in the uniaxial and biaxial cases, respectively. In the triaxial case it should be zero by symmetry, and the difference from zero, representing symmetry-breaking effects, is small. Thus the loading differences between the modes of expansion are quantified in the Mises stress. After the onset of plasticity or the void growth, the Mises stress gets a value of about $\sigma_e = 0.4$ GPa, 0.2 GPa, and 0.1 GPa, in the uniaxial, biaxial, and triaxial cases, respectively, independent of the strain-rate, but with significant fluctuations in this regime. These values are close to the tensile strength or flow stress values of copper, 200-400 MPa, quoted in the literature.[44]

Although the Mises stress captures differences between the loading modes quite well, an even better quantity to study is the ratio between hydrostatic and shear stresses, the *stress-triaxiality*

$$\chi = \sigma_m/\sigma_e, \tag{7}$$

which has been plotted in Fig. 3. In the uniaxial case the stress-triaxiality starts from the value $\chi \simeq 3.0$ and slowly decreases linearly to a value $\chi \simeq 2.8$ until the onset of rapid growth at the yield point. After the rapid increase the stress-triaxiality saturates at $\chi \simeq 11.0 - 16.0$. The stress-triaxiality in the biaxial case starts with a much larger value than in the uniaxial case. It begins at $\chi \simeq 6.0$ and increases linearly to a value $\chi \simeq 8.0$ at the yield point where it grows rapidly to a value of $\chi \simeq 15.0 - 30.0$. These values can be compared with the ratio of the spall and the tensile strength of copper. Previously quoted literature values for them are 6-8 GPa and 200-400 MPa, respectively, giving for their ratio values between 15 and 40, and thus comparable with the stress-triaxiality val-

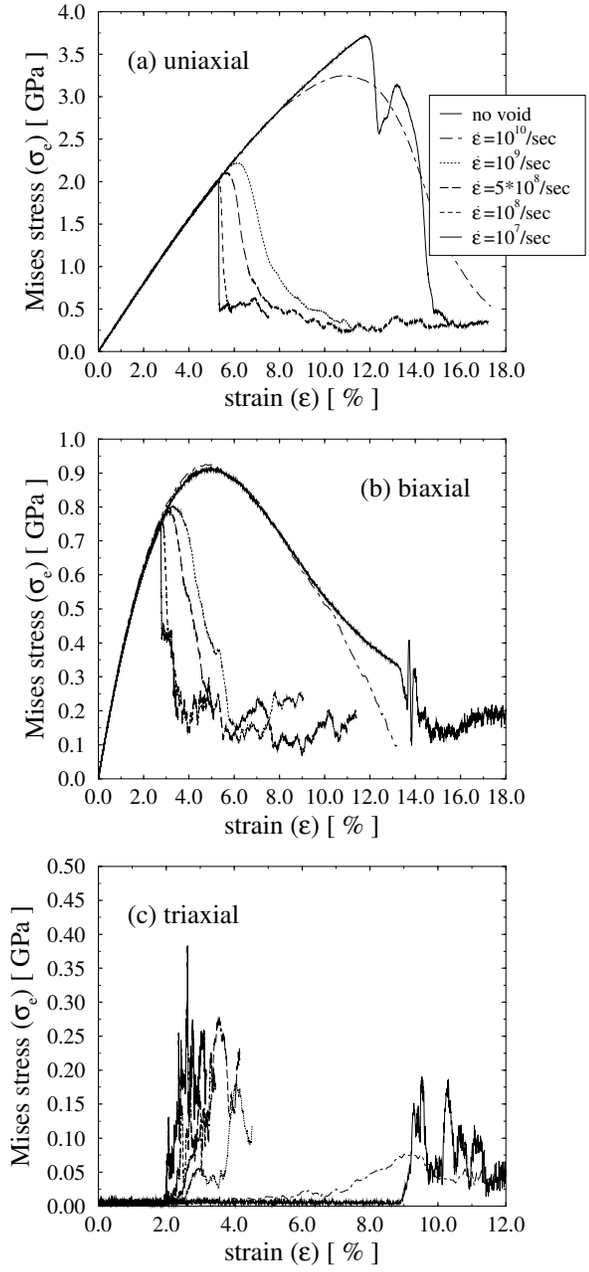

FIG. 2: The Mises stress σ_e versus engineering strain ε from the same simulations as in Fig. 1. In uniaxial and biaxial expansion, the Mises stress rises until the onset of void growth and then it drops to a small value; in triaxial expansion it is always small. See the caption of Fig. 1 for simulation details. (a) Uniaxial, (b) biaxial, and (c) triaxial expansion.

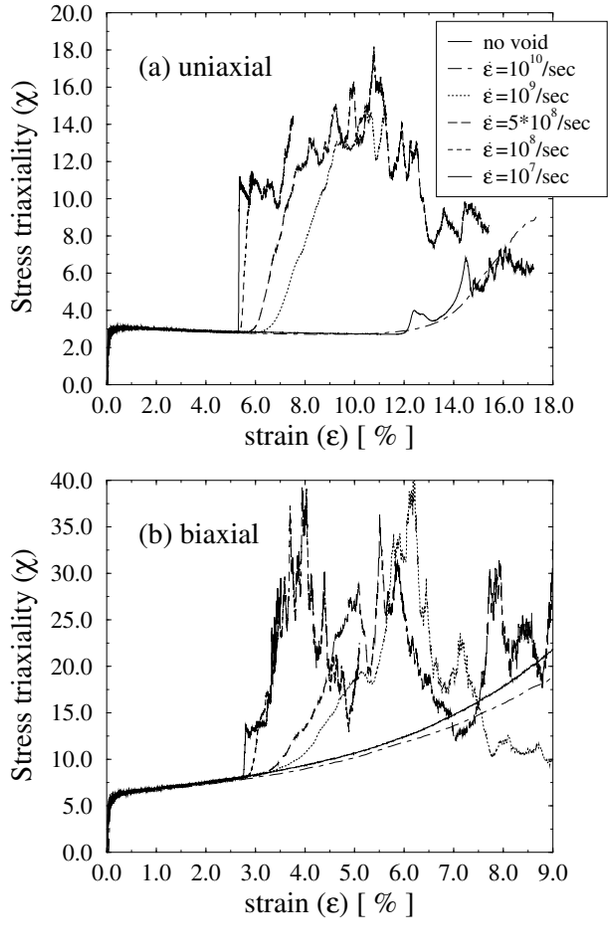

FIG. 3: The stress-triaxiality χ (7) versus engineering strain ε from the same simulations as in Fig. 1. See the caption of Fig. 1 for the details. (a) Uniaxial and (b) biaxial expansion. In triaxial expansion stress-triaxiality is diverging and not defined.

ues here. Since the stress-triaxiality is the mean stress divided by Mises stress, which is equal to zero in the triaxial case until the yield point and very small even after that, the stress-triaxiality is diverging and therefore not plotted here in that case. The stress-triaxiality values in the uniaxial and biaxial cases at the elastic part of the simulation is compared here also with the values one get from the elasticity theory:[45]

$$\chi = \frac{1}{3}\,\frac{C_{11}+2C_{12}}{C_{11}-C_{12}}\;\Xi. \tag{8}$$

$\Xi = 1$ in the uniaxial case and $\Xi = 2$ in the biaxial case. The literature values for the elastic constants of copper are $C_{11} = 168$ GPa and $C_{12} = 121$ GPa.[46] Thus $\chi = 2.9$ and $\chi = 5.8$ in the uniaxial and biaxial cases, respectively, which compare quite well with the simulations presented here. When the elastic constants are derived from the stress-strain curves as $\varepsilon \to 0$, they are close to the actual experimental values: $C_{11} \simeq 162$ GPa, $C_{12} \simeq 121$ GPa and $C_{11} \simeq 168$ GPa, $C_{12} \simeq 124$ GPa in the uniaxial and biaxial cases, respectively.

The critical mean stress, Mises stress, and the stress-triaxiality values where their behaviors start to deviate compared to the elastic ones, or what we call yield points, are summarized in Table I for the strain-rates $\dot{\varepsilon} = 10^9$/sec, 5×10^8/sec, 10^8, and 10^7/sec of the principal strains. In the case of the highest strain-rate $\dot{\varepsilon} = 10^{10}$/sec, the shapes of the stress-strain curves are so much rounded due to over-shooting, that there is no clear point, where the stress-strain curve deviates from the elastic behavior, and thus our definition of the yield point is no longer suitable. In comparing the mean strain values ε_m (as in the Table) at the onset of plasticity for a particular strain rate, one finds that the uniaxial expansion always starts to yield at the least strain, and the hydrostatic expansion, at the greatest strain. There are two effects that contribute to the increase in the plastic threshold as the triaxiality increases. First, the shear component of the applied stress contributes to the resolved shear stress and lowers the threshold for heterogeneous nucleation of dislocations at the void surface.[47] And second, the volumetric strain-rate is lowest in the uniaxial case and the highest in the hydrostatic case. Strain-rate hardening then leads to an increase in the stress value at the onset of plasticity as the triaxiality increases. The difference between the critical strain values when defined as when a behavior deviates from the elastic behavior is nearly negligible and thus independent of whether one uses the criterion from the hydrostatic stress, Mises stress or stress-triaxiality curves. The differences reflect mainly the difficulties in defining the point what we call the yield point. However, we will see later that if the mean stress and Mises stress start to deviate from the elastic behavior with the same ratio as they have during elastic expansion, the stress-triaxiality may deviate a bit later than the other quantities. We shall see later, too, that the onset of plasticity defined from these quantities is very close to where the void starts to grow.

IV. PLASTIC STRAIN AND PLASTIC WORK

After sufficient expansion, the system yields and the mean stress is observed to drop with respect to the elastic response. Then as the simulation box continues to expand, the stress remains roughly constant until the precipitous drop at final failure. In the region of increasing strain but roughly constant mean stress, most of the strain is in the form of plastic strain, a macroscopic measure of the plastic, permanent and irrecoverable deformations in the system. In this Section we study the macroscopic quantities of plasticity such as mean and equivalent plastic strains as well as the plastic work, and in the next Section in more detail what are the actual plastic deformations visible in the void. The concomitant dislocations related to void's shape and volume changes are studied elsewhere.[30,31,47]

In deriving the plastic strain here it is assumed that

TABLE I: The onset of plasticity associated with void growth, as indicated by 3 different criteria: deviation from elastic behavior in the mean stress, Mises stress and stress triaxiality. Their threshold values, together with the corresponding strain values, are tabulated for uniaxial, biaxial and triaxial expansion at the strain rates $\dot{\varepsilon} = 10^9$/sec, 5×10^8/sec, 10^8, and 10^7/sec. In particular, the third and fourth columns show the mean stress values σ and the corresponding mean engineering strain values ε_m, respectively, at the critical or yield point at which the mean stress first deviates from the elastic stress-strain curve. Analogously, the fifth and sixth columns show the yield point as indicated by the Mises stress σ_e and the corresponding mean engineering strain values ε_m, respectively. The seventh and eighth columns show the yield point as indicated by the stress triaxiality χ and the corresponding mean engineering strain values ε_m, respectively. Note the small but significant differences in the yield point as indicated by these three different criteria. The error bars of the values are of the order of last reported digit. The details of the simulations are in the caption of Fig. 1 and the curves, from which the yield data have been calculated, are plotted in Figs. 1-3. Note that, as expected, the Mises stress is small and erratic in the triaxial case, so those Mises and stress-triaxiality data are not tabulated.

$(\varepsilon_x, \varepsilon_y, \varepsilon_z)$	$\dot{\varepsilon}$ (sec^{-1})	σ (GPa)	ε_m (%)	σ_e (GPa)	ε_m (%)	χ	ε_m (%)
$(\varepsilon, 0, 0)$	10^9	5.87	1.85	2.12	1.87	2.78	1.92
$(\varepsilon, 0, 0)$	5×10^8	5.82	1.84	2.09	1.84	2.79	1.84
$(\varepsilon, 0, 0)$	10^8	5.65	1.77	2.01	1.77	2.80	1.77
$(\varepsilon, 0, 0)$	10^7	5.60	1.77	2.00	1.77	2.79	1.77
$(0, \varepsilon, \varepsilon)$	10^9	6.50	2.02	0.79	2.02	8.29	2.02
$(0, \varepsilon, \varepsilon)$	5×10^8	6.50	2.02	0.79	2.02	8.23	2.02
$(0, \varepsilon, \varepsilon)$	10^8	6.03	1.85	0.75	1.87	8.08	1.86
$(0, \varepsilon, \varepsilon)$	10^7	5.96	1.83	0.74	1.82	8.02	1.82
$(\varepsilon, \varepsilon, \varepsilon)$	10^9	7.25	2.30				
$(\varepsilon, \varepsilon, \varepsilon)$	5×10^8	7.25	2.30				
$(\varepsilon, \varepsilon, \varepsilon)$	10^8	6.50	2.00				
$(\varepsilon, \varepsilon, \varepsilon)$	10^7	6.33	1.94				

the tetragonal symmetry is approximately preserved and thus the off-diagonal terms of the stress tensor are negligible. Following the literature we separate the strain increment $d\varepsilon = \dot{\varepsilon}\, dt$ into elastic and plastic parts.[48] Thus by definition the plastic strain increment becomes

$$\dot{\varepsilon}^P_{\alpha\beta}\, dt = \dot{\varepsilon}^{tot}_{\alpha\beta}\, dt - \dot{\varepsilon}^E_{\alpha\beta}\, dt, \tag{9}$$

where $\dot{\varepsilon}^{tot}_{\alpha\beta}\, dt$ is the total increment of the strain. Below we use $\dot{\varepsilon}$ instead of $\dot{\varepsilon}\, dt$ since dt can be divided from both sides of Eq. (9). The total strain increment is an input parameter in these strain-controlled simulations. It is given by the strain-rate matrix $\dot{\mathcal{E}}$. The compliance $\mathcal{S}$ relating the elastic strain increment to the stress increment is derived from the stress-strain curves in the elastic region by:

$$\dot{\varepsilon}^E_{\alpha\beta}(\sigma_{\alpha\beta}) = \mathcal{S}\dot{\sigma}_{\alpha\beta}. \tag{10}$$

The stress matrix $\sigma_{\alpha\beta}$ is calculated each time-step using Eq. (3). The elastic compliance tensor $S(\sigma_{\alpha\beta})$ is retrieved from the elastic part of the stress-strain curve of the cases without the void as follows. Due to the nonlinearity of the stress-strain curve we have not only retrieved the slope of it, which would give $3B = C_{11} + 2C_{12}$, where B is the bulk modulus, but fitted a fourth order polynomial to the strain versus stress curve, whose derivative gives us $1/3B^{-1}(\sigma_m)$. It should be mentioned, too, that in the derivation of the bulk modulus the mean total logarithmic strain is used instead of the engineering principal strain used in the plots of this Article. Similarly the term $C' = \frac{1}{2}(C_{11} - C_{12})$ is derived using a fourth order polynomial in the mean strain versus Mises stress curve giving $1/C'$. Note, that when C' is derived from the plot using mean strain there are prefactors 1/3 and 2/3 for C' in the uniaxial and biaxial cases, respectively. Since[43]

$$B = \frac{1}{3}(C_{11} + 2C_{12}), \tag{11}$$

$$C' = \frac{1}{2}\left(C_{11} - C_{12}\right), \tag{12}$$

$$S_{11} = \frac{C_{11} + C_{12}}{(C_{11} - C_{12})(C_{11} + 2C_{12})}, \tag{13}$$

and

$$S_{12} = \frac{-C_{12}}{(C_{11} - C_{12})(C_{11} + 2C_{12})}, \tag{14}$$

we get for S_{11} and S_{12}

$$S_{11} = \frac{1}{9B} + \frac{1}{3C'}, \;\; S_{12} = \frac{1}{9B} - \frac{1}{6C'}. \tag{15}$$

Using the $S_{11}(\sigma_m)$ as $S_{\alpha\alpha}(\sigma_m)$ and $S_{12}(\sigma_m)$ as $S_{\alpha\beta}(\sigma_m)$ due to the symmetry and neglecting off-diagonal terms, which are small compared to the diagonal ones, we get all the necessary terms for $S(\sigma_m)$, and thus $\dot{\varepsilon}^E_{\alpha\beta}(\sigma_m)$ from Eq. (10). Note, that since the σ_m is used as a parameter

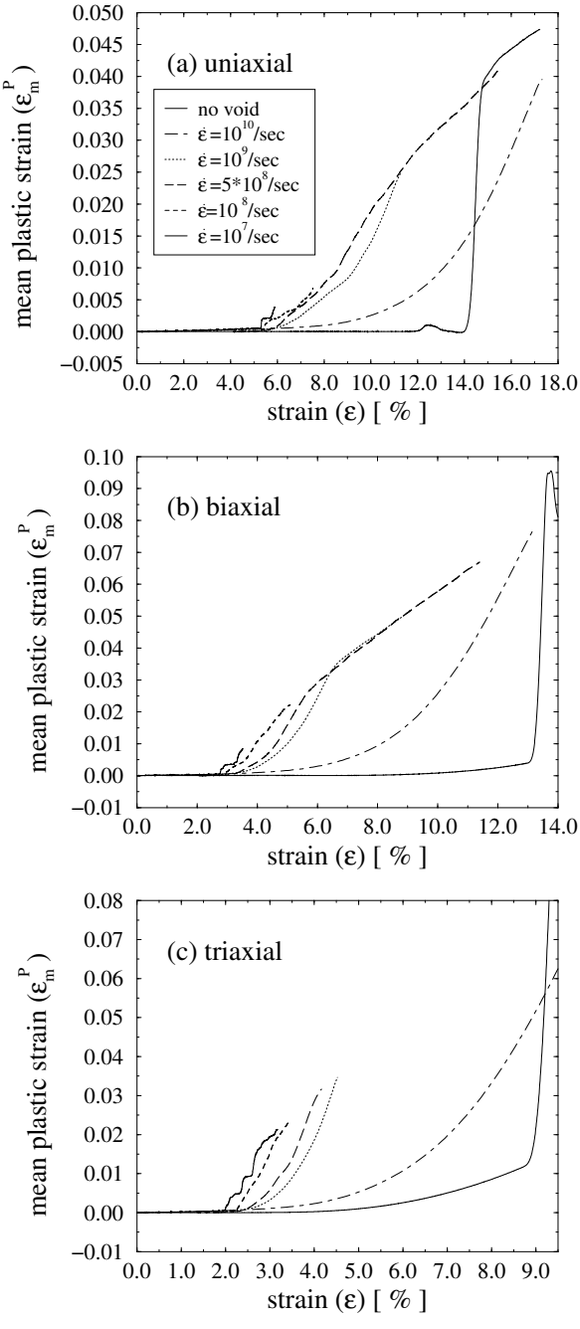

FIG. 4: Mean plastic strain ε_m^P, calculated using Eq. (16), versus engineering strain ε from the same simulations as in Fig. 1. See the caption of Fig. 1 for the details. (a) Uniaxial, (b) biaxial and (c) triaxial expansion.

instead of $\sigma_{\alpha\beta}$, Mises stress must be mapped with the mean stress when finding the corresponding C'. This was done again by fitting the Mises vs. mean stress curves with fourth order polynomials.

Subtracting the elastic strain from the total strain as in Eq. (9) we get the mean plastic strain increment

$$\dot{\varepsilon}_m^P = \frac{1}{3}\sum_\alpha \dot{\varepsilon}_{\alpha\alpha}^P, \tag{16}$$

which time-integral is plotted in Fig. 4 for all the loading modes and strain-rates. In these plots one sees that after the yield point the mean plastic strain first increases roughly exponentially, although the region is too small to be definitive, and thenceforth roughly linearly. Note that the mean plastic strain is not the equivalent plastic strain commonly used in plasticity, which will be defined below, but a measure of the porosity. This will be studied in the next Section, where the mean plastic strain will be compared with the growth of the volume of the void.

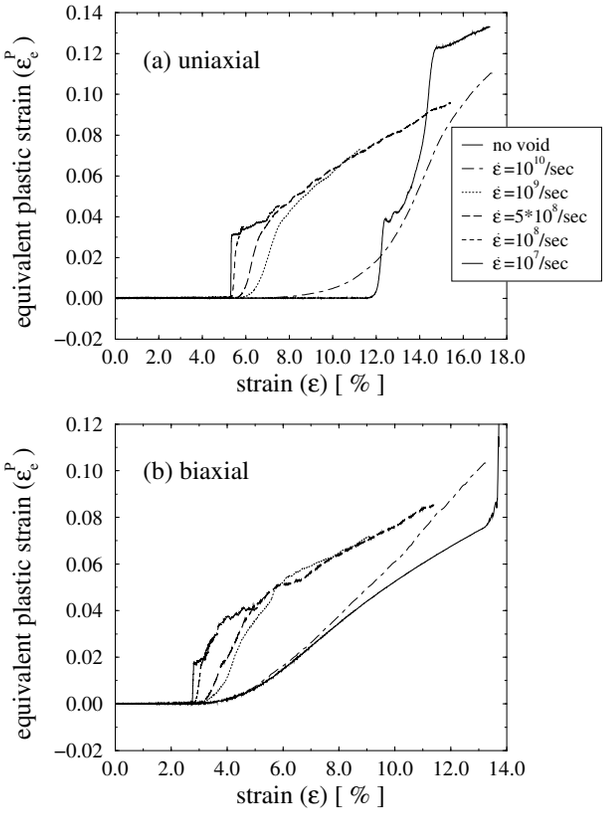

FIG. 5: Equivalent plastic strain ε_e^P, calculated using Eq. (17), versus engineering strain ε from the same simulations as in Fig. 1. See the caption of Fig. 1 for the details. (a) Uniaxial and (b) biaxial expansion.

As in the case of stress, the deviatoric part of plastic strain, the *equivalent plastic strain*, can be derived in the tetragonal case:

$$\int \dot{\varepsilon}_e^P\, dt = \frac{1}{3}\left\{ 2\sum_{\alpha>\beta}\left(\int \dot{\varepsilon}_{\alpha\alpha}^P\, dt - \int \dot{\varepsilon}_{\beta\beta}^P\, dt\right)^2 \right\}^{1/2}. \tag{17}$$

Since only the principal stresses, the diagonal terms of the stress, are taken into account in Eq. (10) and we

have only two different terms in $\mathcal{S}$ generally, $S_{\alpha\alpha}$ and $S_{\alpha\beta}$, the equivalent plastic strain equals zero during the whole simulation in the triaxial cases. In the uniaxial and biaxial cases the equivalent plastic strain is plotted in Fig. 5.

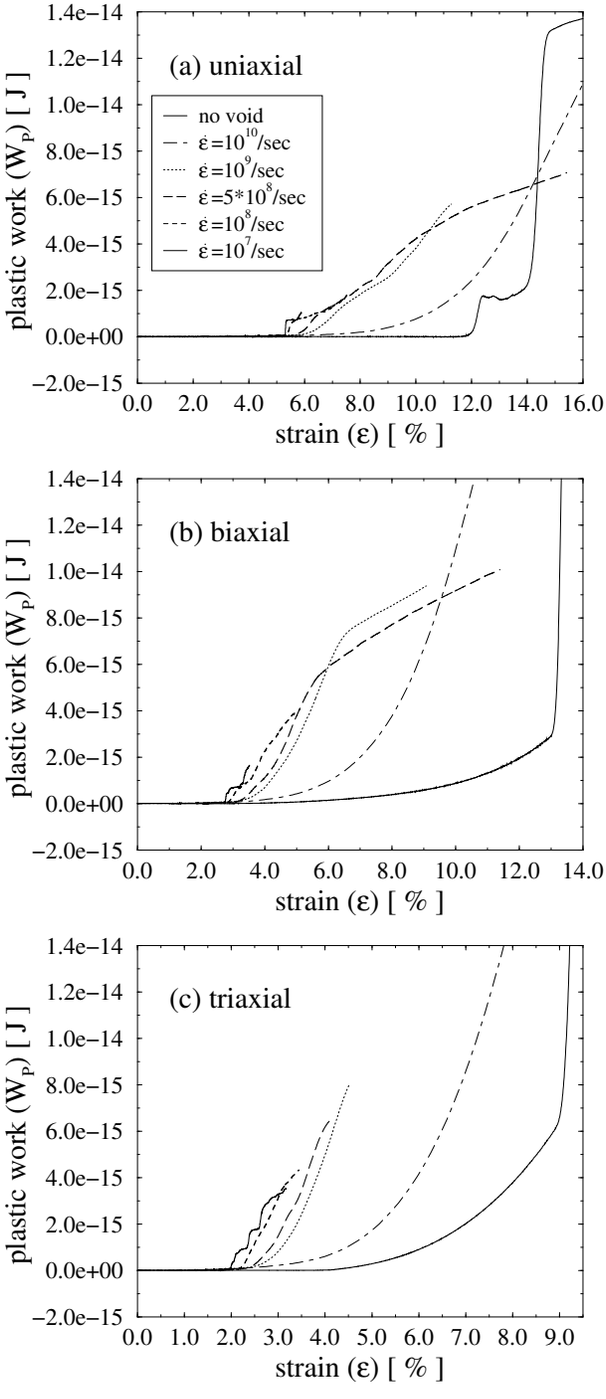

FIG. 6: Plastic work W_P, calculated from Eq. (18), versus engineering strain ε from the same simulations as in Fig. 1. See the caption of Fig. 1 for the details. (a) Uniaxial, (b) biaxial, and (c) triaxial expansion.

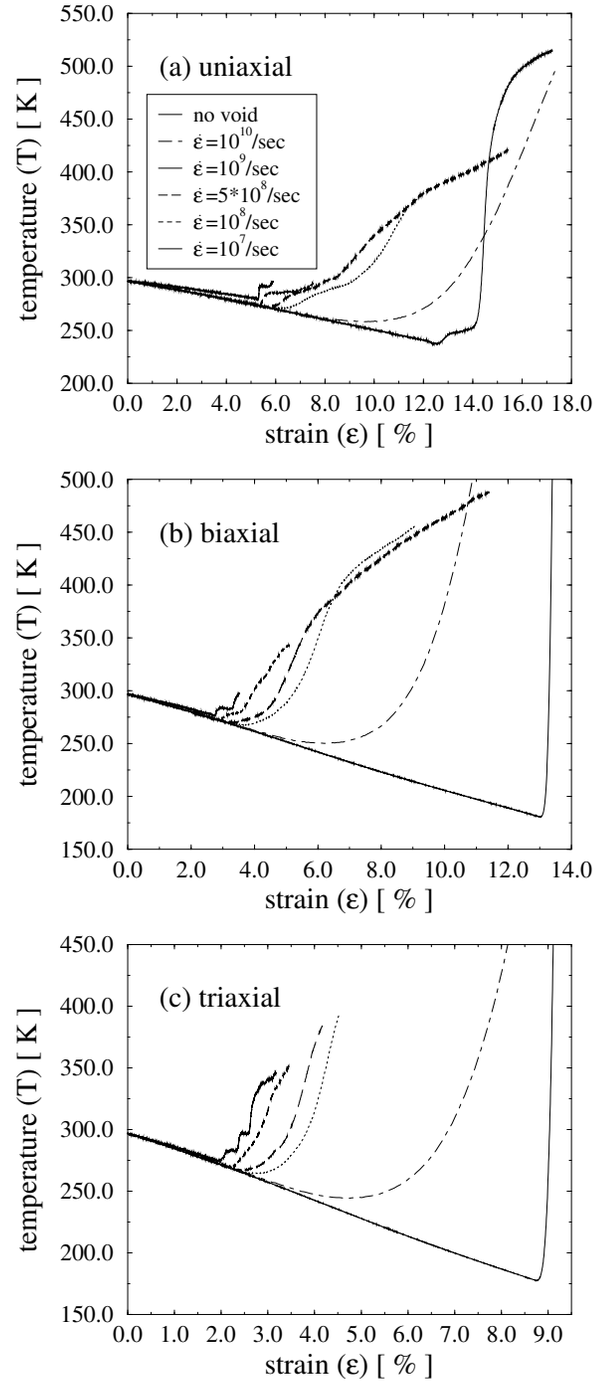

FIG. 7: Temperature T, versus engineering strain ε from the same simulations as in Fig. 1. Compare with the plastic work plotted in Fig. 6. See the caption of Fig. 1 for the details. (a) Uniaxial, (b) biaxial, and (c) triaxial expansion.

Now, once the tensors for both the stress and the plastic strain are derived, (actually only the diagonal terms of the plastic strain are needed), the plastic work can be calculated,

$$W_P(t) = \sum_\alpha \int \dot{\varepsilon}^P_{\alpha\alpha} \sigma_{\alpha\alpha}\, dt, \tag{18}$$

(see Fig. 6). It should be compared with the temperature from the same simulations, Fig. 7. Note, that in these simulations, when the dilational strain is applied, the thermostat is turned off and thus the temperature is allowed to change. First the system cools in the elastic regime due to adiabatic cooling on expansion, but when plastic deformations begin, work is done in the system resulting in heating. We find that the increase in plastic work does not match exactly with the temperature. In principle we expect several effects to contribute to this difference: the surface energy of the void, the defect formation energies for dislocations and point defects, further adiabatic cooling, and any error in calculating the elastic energy from the stress. Using the best data available to bound the contributions from surface, defect and adiabatic cooling energies, we find that there remains an energy deficit that we attribute to an error in the calculated elastic energy. The error comes from the use of the average stress despite stress inhomogeneity in the system due to the void: in the plastic work the product of plastic strain and stress is calculated with averaged quantities, while in the temperature the product is calculated at level of each atom and averaged afterward.

V. VOID EVOLUTION

A. Growth of the Void

We now consider the volume and shape evolution of the void. During the MD simulations undergoing expansion, the surface of the void is determined by finding individual atoms that belong to the surface. This is done by creating a fine two-dimensional mesh, in which each mesh point corresponds to spherical angular coordinates (ϕ, θ). An atom is found to represent the surface at each point of the mesh, with some atoms representing multiple mesh points. In particular, taking the origin to be the center of the void, within the solid angle associated with each mesh point, the atom that is closest to the origin is defined to be the surface atom at that mesh point. There are, however, some uncertainties related to this method. If the mesh is too dense with its size diverging it can capture almost all the atoms in the system. On the other hand if it is too sparse, it may neglect some surface atoms, especially when void is anisotropic, non-spherical, and has some sharp edges in it. Therefore we introduced a width to each of the atoms by drawing a circle around it that implies a width $(d\phi, d\theta)$ to the angles, so that one atom can occupy several mesh points in a fine mesh. We have typically 75-100 points for each angular coordinate, giving a total of 5625-10000 mesh points. In the surface of the void there are typically few thousand atoms. Besides introducing the width to the atoms, we also select atoms based on their radial distance: if an atom has much larger radial distance r compared to its neighbors it is neglected in order not to capture atoms that do not belong to the surface.

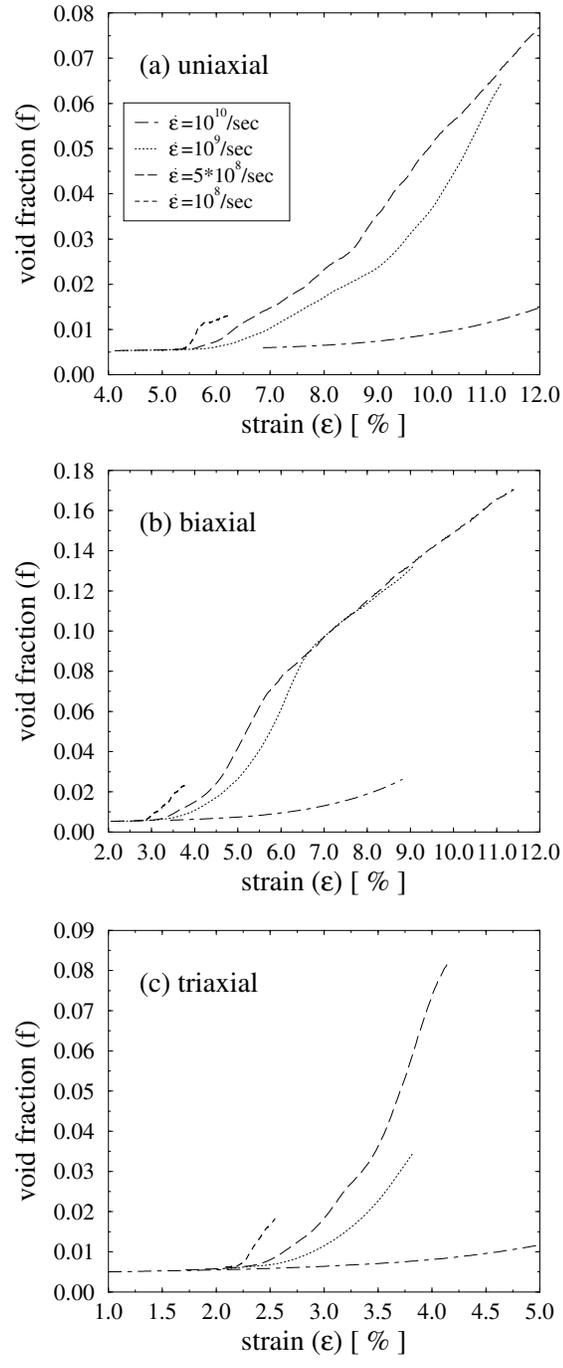

FIG. 8: Void volume fraction versus engineering strain ε. The evolution of the ratio of the void volume to the total box volume is plotted for strain-rates $\dot{\varepsilon} = 10^{10}$/sec, 10^{9}/sec, 5×10^{8}/sec, and 10^{8}/sec. See the caption of Fig. 1 for additional details. (a) Uniaxial, (b) biaxial, and (c) triaxial expansion.

Once the surface atoms are identified, the surface is tessellated using a generalization of the Delaunay triangulation method.[49] The Delaunay triangulation is an optimal triangulation of a collection of points–in our case atoms–on the plane. It is optimal roughly in the sense that the aspect ratio of the triangles is as near to unity

as possible; more precisely, the Delaunay theorem guarantees that there is a unique (up to degeneracy) triangulation such that if any triangle in the triangulation is circumscribed by a circle, none of the other points will be in the interior of the circle. The Delaunay theorem, as formulated, does not apply to points on a curved surface. In fact, there appears to be a topological obstruction to the existence of a unique, optimal triangulation on a closed surface when the Euler character is non-zero. Nevertheless, it is possible to extend the Delaunay triangulation algorithm to achieve a locally optimal triangulation almost everywhere. The approach we have taken is to project the points patchwise onto flat surfaces. In particular, stereographic projections are used to project the upper and lower hemispheres separately onto planes. Cylindrical coordinates are used to project the equatorial region to a cylinder. The Delaunay algorithm is used to triangulate each of these projected regions. The patches overlap at latitudes of $\pm 45^\circ$ where the projections are not too distorted. The three patches are sewn together using a simple advancing front triangulation at the boundaries.

Using this triangulation, the volume of the void can be calculated precisely by summing up the volumes of the tetrahedra with one apex at the center of the void and the opposing face on the void surface. As we shall see below, the void shape evolves to be far from spherical. Therefore the approximation of the void surface by triangles captures the shape better than just assuming it to be spherical and using only the solid angles and radial distances of a sphere, when calculating the volume of the void. An advantage of this method is that if some atom, which should be taken into account, is missing from the surface of the void, its position is filled with the triangles created by its neighboring atoms, and thus the "hole" is well approximated by its neighbors.

In Fig. 8 the porosity or the ratio between the volume of the void and the total volume of the system,

$$f = V_{void}/V, \tag{19}$$

is plotted for a fraction of the simulations of the strain-rates $\dot{\varepsilon} = 10^{10}$/sec, 10^9/sec, 5×10^8/sec, and 10^8/sec. It should be noted that in order to get information about the positions of the atoms for the strain values of the interest (*i.e.*, close to and after the onset of plasticity) the calculations were restarted from already expanded system. After the restart the expansion was applied with the same strain-rate as earlier but now to the already expanded system, thus the strain-rate was increased by a few percent compared to the original [since $\mathcal{H}_0$ in Eq. (2) was the restart value]. Therefore these simulations are not precisely comparable with the ones plotted in Figs. 1-7, where the continuum quantities are shown. In these plots, as for the mean plastic strain, in most cases first the void grows exponentially and then (if the calculation has been carried out that long) it changes to a linear growth, see especially Fig. 8(b) and the strain-rates 10^9/sec and 5×10^8/sec there. The cross-over to the linear growth happens at the same point as the rate of decrease of the mean stress slows. Although it is beyond the scope of this Article to go into the analysis, the reduction in the growth rate coincides with the point at which the dislocation density along the shortest distance between the void and its periodic image (at the apices of the faceted void, cf. Section V B) reaches saturation, and the nature of the dislocation activity changes dramatically. This can be interpreted as a finite size effect as the void approaches the boundary of the simulation box. The shapes of the porosity curves as a whole can be compared with the mean plastic strain plotted in Fig. 4. Although the volume of the void is not calculated throughout the whole simulation, one sees easily, that there is correspondence between mean plastic strain and the volume of the void.[50] There is of course an offset at the elastic part of the simulations, since mean plastic strain equals zero then, but the initial volume of the void is finite. The correspondence will be revisited and studied more carefully in Section VI. However, it can be concluded already here that the macroscopic quantity mean plastic strain captures the microscopic behavior of the void growth very well. Effects such as the excess volume associated with defects are negligible. This also means that the matrix material is plastically incompressible, the dilation comes from the void growth, and thus it is consistent with the Gurson type of continuum models.[16]

B. Shape Evolution of the Void

Let us now look at the shape evolution of the void in more detail. In Fig. 9 snapshots of the void are shown from uniaxial expansion at the strain-rate $\dot{\varepsilon} = 10^8$/sec. There are several interesting aspects in the snapshots. In the first two snapshots at strains $\varepsilon = 5.05\%$ and 5.26% when the system still behaves elastically, the void is expanded in the x-direction, which is the direction of the strain. However, after that the void makes a rapid shape change and becomes more extended in the transverse y and z-directions, *i.e.*, the strain-free directions, than x-direction. This prolate-to-oblate transition may be counterintuitive, but the behavior has been observed previously in continuum calculations,[27,51,52] and it has been related to the appearance of shallow dimples in the fractography studies of ductile fracture surfaces in low triaxiality conditions. See also studies of non-spherical voids.[53,54] For example, Budiansky *et al.* investigated void shape change in a non-linear viscous plastic flow model. They explained the oblate growth of voids under uniaxial loading as due to a non-linear amplification of the shear stress on the surface of the void, with the maximal void growth rate at the locations of maximal Mises stress: the equator. Their analysis does not apply directly to our simulations since they neglect elasticity, and the prolate-to-oblate transition takes place in our simulation early in the development of plastic flow, well before it should be sensitive to the strain hardening exponent (the non-linearity in the model of Budiansky *et*

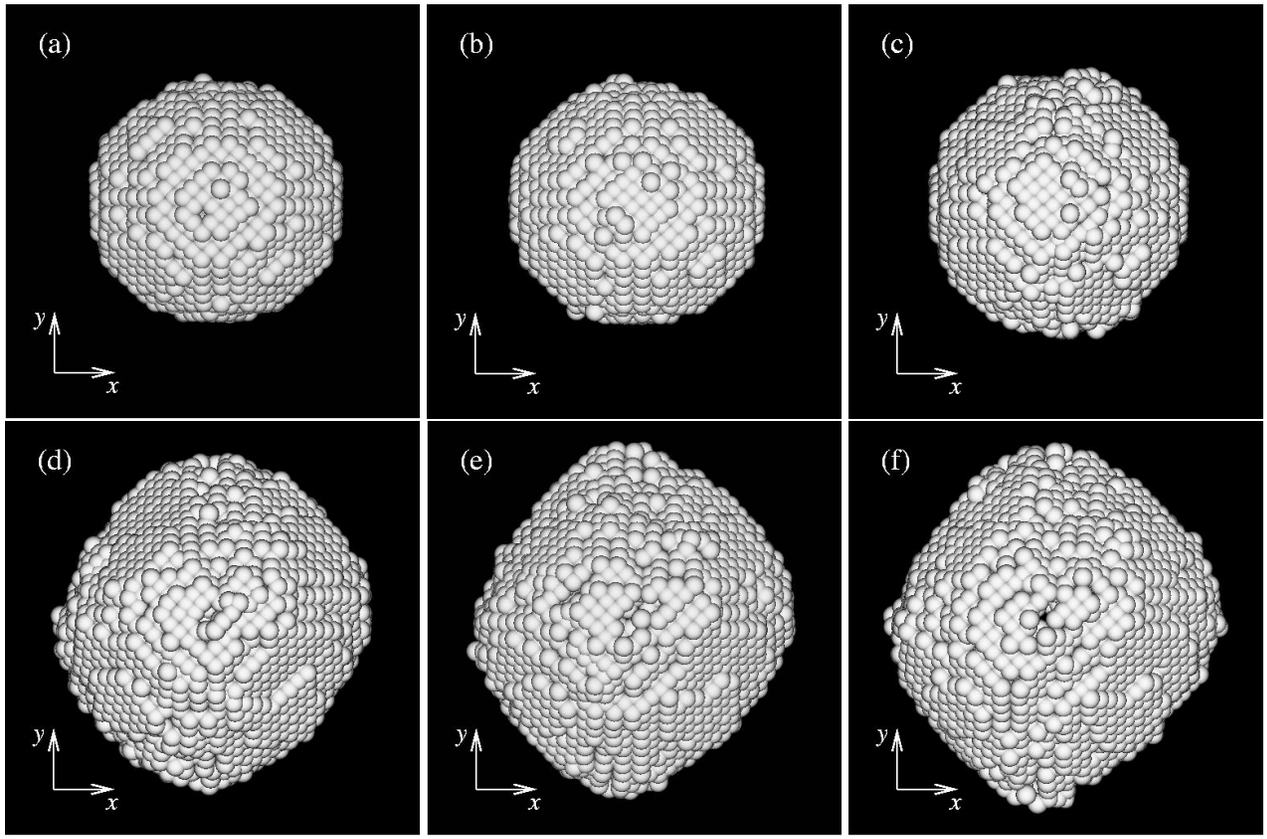

FIG. 9: Snapshots of the atoms comprising the surface of the void during uniaxial expansion with $\varepsilon_x = \varepsilon$, $\varepsilon_y = \varepsilon_z = 0$. The simulation box is oriented along $\langle 100 \rangle$ directions, so that the z-axis is out of the paper. The strain-rate is $\dot{\varepsilon} = 10^8$/sec. See the caption of Fig. 1(a) for additional details. The panels show snapshots at different strains: (a) $\varepsilon = 5.05\%$ (b) $\varepsilon = 5.26\%$ (c) $\varepsilon = 5.47\%$ (d) $\varepsilon = 5.68\%$ (e) $\varepsilon = 5.89\%$ (f) $\varepsilon = 6.10\%$

al.). Nevertheless, the same localization of plastic flow to the equator of the void does appear in our simulations. Following some additional expansion beyond the transition, the void begins to become faceted, as visible in the last three snapshots. It should be mentioned that the anisotropy visible in this uniaxial case is less pronounced in the biaxial case. The cases with the hydrostatic loading are the most isotropic and the octahedral shape, somewhat visible in Fig. 9(f), becomes more pronounced.[31] The octahedral shape has been seen in spallation experiments in the FCC metal aluminum,[55] and also in experiments on the equilibrium void shape of another material, silicon, too, where it has been used to calculate anisotropic surface energies through an inverse Wulff construction.[56] In void growth associated with dynamic fracture in copper, several effects contribute to the faceting: the low surface energy and high ad-atom energy of the {111} surfaces common to FCC metals, the high anisotropy of the copper elastic constants (A=3.21), and the {111} dislocation glide systems. These effects are analyzed in detail elsewhere.[47]

In order to characterize the shape change of the void not only qualitatively and visually, but also quantitatively, multipole moments of the void shape are calculated. To the best of our knowledge, this is the first time that multipole moments have been used to characterize surface shape. They are a powerful way to quantify the evolution of the complex surface containing thousands of atoms, and they are suitable for use in continuum models and experimental void characterization as well. Using spherical harmonics,

$$Y_{lm}(\vec{r}) \equiv Y_{lm}\{\theta(\vec{r}), \phi(\vec{r})\}, \tag{20}$$

expressed as polynomials of Cartesian coordinates, in contrast to more commonly used trigonometric forms,[57] we are able to define different multipole moments of the void based on its surface atoms:

$$Q_{lm} \equiv \tfrac{1}{\bar{r}^2} \int Y_{lm}(\theta, \phi)\, r^2(\theta, \phi)\, d\Omega, \tag{21}$$

where the mean square radius $\bar{r}^2 = \frac{1}{4\pi} \int r^2(\theta, \phi)\, d\Omega$. This is in contrast to the volume integral more commonly used when calculating multipole moments. The axial index of the moment ranges $m = -l, \ldots, l$, and for each m except $m = 0$, Q_{lm} has both real and imaginary parts. Here we concentrate on $l = 1, 2, 3$, and 4. Only the positive moments of m are calculated, since the negative ones are related by

$$Q_{l,-m} = (-1)^m Q^*_{lm}. \tag{22}$$

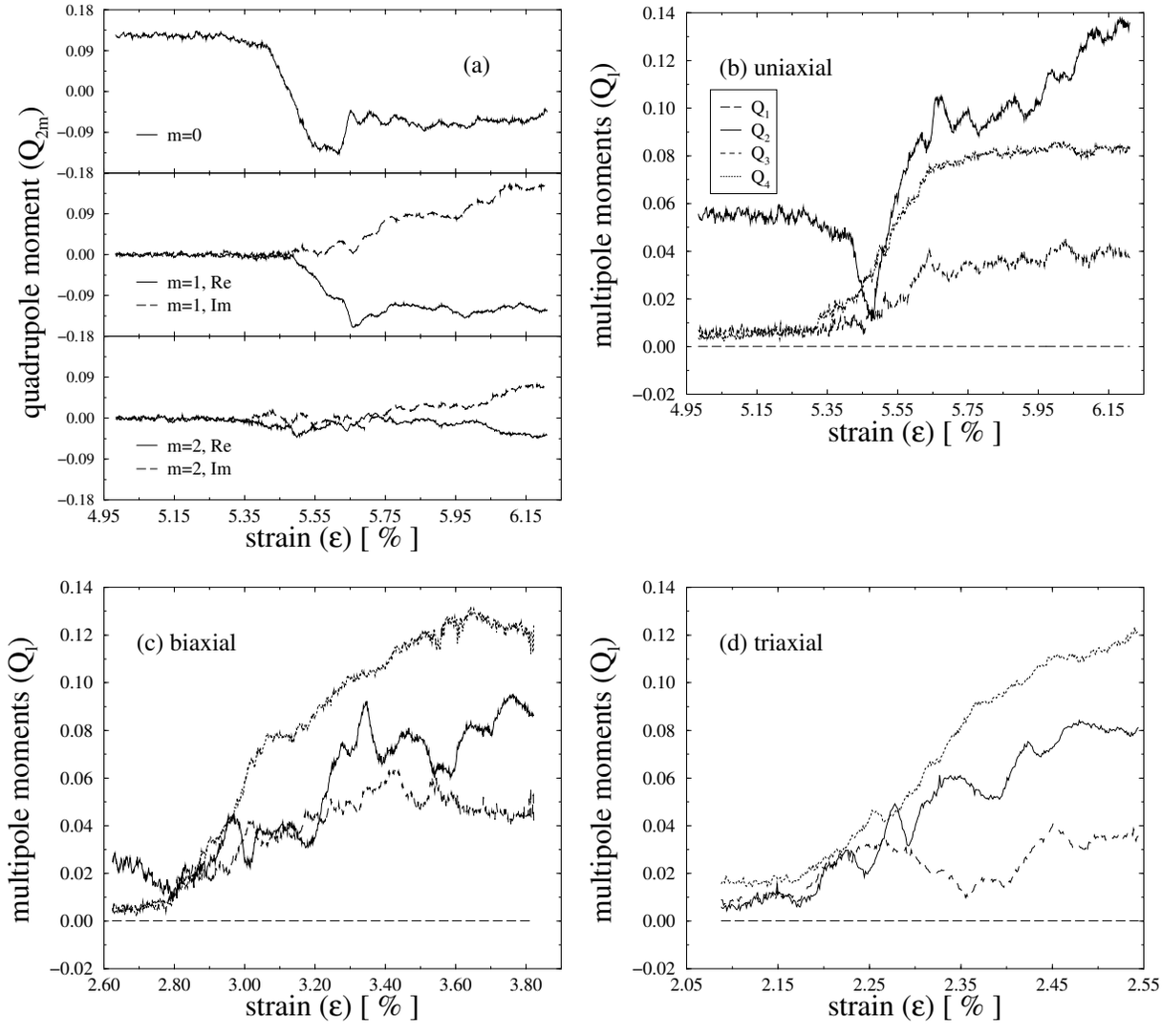

FIG. 10: Multipole moments of the void surface calculated using Eq. (21). (a) Quadrupole moment Q_{2m} with $m = 0, 1, 2$ for uniaxial expansion at $\dot{\varepsilon} = 10^8$/sec. Note, that the principal axis of the coordinates [z-coordinate in Eq. (A2)] is in the direction of the strain here (elsewhere the x-direction). (b)-(d) The moments Q_l for $l = 1, 2, 3, 4$ in (b) uniaxial, (c) biaxial, and (d) triaxial cases. They are calculated using Eq. (23) and the strain-rate $\dot{\varepsilon} = 10^8$/sec. See the caption of Fig. 1 for details of the simulations.

In all 24 different terms are calculated. The polynomial forms used here of the moments are listed in the Appendix.

The moments Q_{lm} are not rotationally invariant, but depend on the way the coordinates x, y, and z are chosen. The set of $(2l + 1)$ moments at fixed l form an irreducible representation of the SO(3) rotation group, and are mixed by rotations according to the usual transformation rules. They may be combined into a single rotationally invariant combination for each l according to

$$Q_l = \left[\frac{1}{2l+1} \sum_{m=-l}^{l} |Q_{lm}|^2 \right]^{1/2} , \qquad (23)$$

see *e.g.* Ref. 59. Their use drastically reduces the amount of data to be shown. Only the positive m's are needed for Q_l due to the square of the norm of Q_{lm} and Eq. (22).

Technically the calculation of the multipole moments has been done using the information about the shape of the void obtained from the surface triangulation procedure explained earlier. As in the calculation of the void volume, some refinements have been introduced to reduce the uncertainty in the values of the moments that arises from single atoms near the threshold for inclusion as surface atoms. These borderline atoms can appear intermittently on the void surface during the growth, and the tessellation is used to minimize their effect on the moments. In calculating the volume of the void the triangulation gave one face of the tetrahedra that acted as small volume elements for the total volume. Here the tri-

angulation is used to weight the atoms by the amount of solid angle associated with each surface atom. In particular, each triangle in the tesslation contributes one third of its projected solid angle to each of the three atoms that make up its vertices, where the solid angle of a triangle is computed using the formula $\delta\Omega = A_1+A_2+A_3-\pi$, where $A_i = \arccos\left(\frac{c_i - c_{i+1}c_{i+2}}{\sqrt{1-c_{i+1}^2}\sqrt{1-c_{i+2}^2}}\right)$ and $c_i = \hat{x}_{i+1}\cdot\hat{x}_{i+2}$ for $i = 1, 2, 3$ (mod 3) and where $\hat{x}_i$ is the unit vector in the direction of the i^{th} vertex of the triangle.[60] The weight of each atom is the sum of these solid angle contributions. This reduces the sensitivity of moments to the atomic discretization of the surface, since evanescent atoms that occasionally appear and disappear from the fluctuating surface only make a small, local change to the value of r^2. It may be of interest to note that in the course of the development of these surface multipole moments, several different variations on the definition of the moments were tried. The definition presented here (21) produced substantially less noise (up to a factor of 5 less noise) than the other definitions we tried, even though they all showed the same trends in the shape evolution. Using these weights for the atoms and after normalizing each atom's (x, y, z) coordinate by its distance $r = (x^2 + y^2 + z^2)^{1/2}$ from the center of the void all the terms in Eqs. (A1)–(A4), and Eq. (23), are calculated. The center of the void is defined to be the point where the three components of Q_{1m}, as given by Eq. (A1), are zero.

Due to space limitations, only a fraction of the multipole moment data is shown here. In Fig. 10(a) the quadrupole moments Q_{2m} for all the positive m of the void are shown in the uniaxial case for the strain-rate $\dot{\varepsilon} = 10^8$/sec. This is the same simulation as the snapshots in Fig. 9. Indeed, the quadrupole moments are able to represent numerically the shape changes one sees in the snapshots. It should be noted that following convention the z-direction in the formulas in Eq. (A2) is now the direction of the strain, and x and y are the unstrained directions. Previously the coordinates have been such that x is the direction of the load. In Figs. 9(a) and (b) at strains $\varepsilon = 5.05\%$ and 5.26% the void is elongated to the direction of the load, which is visible as $Q_{20} > 0$. Between strains $\varepsilon = 5.47\%$ [Fig. 9(c)] and 5.68% [Fig. 9(d)] the void is extended more transverse to the direction of the strain, thus $Q_{20} < 0$, and later it starts to becomes more of octahedral shape and the absolute value of Q_2 saturates.

Figures 10(b)–(d) show the rotational invariant multipole moments Q_l, Eq. (23), in cases with uniaxial, biaxial, and triaxial loading, respectively. Each of the cases has strain-rate $\dot{\varepsilon} = 10^8$/sec. In the plots it is clear that the behavior that the quadrupole moment has first a non-zero value and then makes a rapid dip but returns back to a non-zero value due to the transverse elongation is the strongest in the uniaxial case. On the other hand the octahedral shape measured by the Q_4 is more pronounced in the biaxial and triaxial cases than in the uniaxial case as explained qualitatively earlier. Hence we find that the multipole moments introduce a good method to measure the shape changes of the void. The non-zero values for Q_3, as well as Q_2 in other cases than uniaxial, indicate that the void is not (cubically) symmetric in these simulations. It should be mentioned that these first four moments are enough to characterize the shapes of the void and the higher moments contain little relevant information. This was checked by creating a three dimensional surface based on the moment values and drawing it in the same figure with the actual positions of the surface atoms using a standard commercial visualization program. The surfaces overlapped very well.

VI. SUMMARY OF THE UNIAXIAL CASE

Based on the data shown earlier in this Article for the shape and volume changes of the void as well as the stress-strain behavior and the stress-triaxiality, it is evident that the uniaxial loading raises many interesting aspects to be studied in more detail. Therefore we now concentrate on the uniaxial case when summarizing how the void evolves and how the evolution is related to the stress-triaxiality as the system is expanded. By plotting most of the measured values together in one figure for the uniaxial simulation at the strain-rate $\dot{\varepsilon} = 10^8$/sec, it is possible to compare the evolution sequence and investigate causality, see Fig. 11(a). For clarity, we have chosen not to plot many quantities in the figure, *e.g.* plastic strain, plastic work, and temperature. However, their concomitant behaviors are included in the verbal explanation below and shown in previous figures. The data shown in this figure are from the restarted simulation (see the explanation near Fig. 8), as are the data in Figs. 8-10. The mean stress and stress-triaxiality data are from that simulation, too, and thus are different from the data shown in Figs. 1(a) and 3(a). In any case, the overall behavior stays the same as well as the other details as the system size, *etc.*

The evolution of the void and the system's stress-strain behavior can be divided in three or even four different regions. The first region is when the system expands elastically. The mean and Mises stresses increase smoothly, nearly linearly, and the stress-triaxiality stays nearly constant. Through the elastic region the void volume fraction remains nearly constant, too. It is not exactly constant, since due to the free surface of the void, the elastic expansion is a bit greater at the surface of the void compared to the total system. Trivially the mean and equivalent plastic strains as well as the plastic work are equal to zero in the elastic region, and temperature decreases in the system. The quadrupole moment has a non-zero value because of the elongation in the direction of the strain.

The second region begins at what we call the yield point, *i.e.*, the onset of rapid growth of the void facilitated by plastic deformation. Heterogeneous nucleation of dislocations at the void surface is the primary mech-

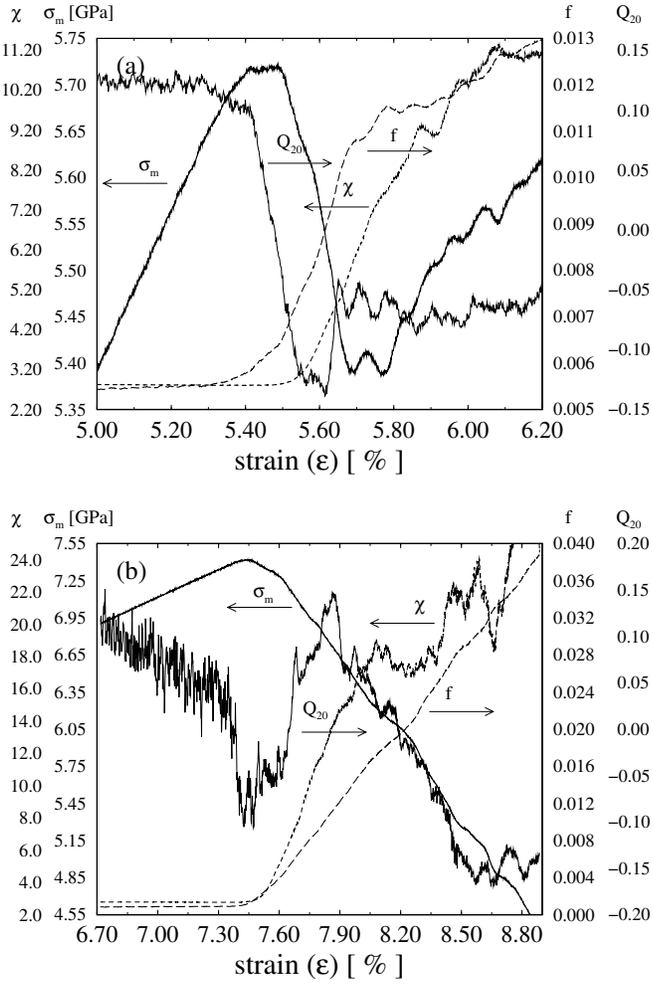

FIG. 11: (a) The mean stress σ_m (thick solid line), stress-triaxiality χ (dotted line), volume fraction f of the void (dashed line), and the quadrupole moment Q_{20} (thin solid line) from the simulation with uniaxial expansion at $\dot{\varepsilon} = 10^8$/sec. See the captions of Figs. 1, 3, 8, and 10 for the details. (b) As a comparison the same measures as in (a), but now for the case having an initial void radius of 1.1 nm and 863 543 atoms in the system undergoing uniaxial expansion at the same $\dot{\varepsilon} = 10^8$/sec.

anism for plasticity in the simulation, and thus it is at this point that the measured quantities start to deviate from their elastic behavior. The mean stress begins to plateau here, but fluctuating somewhat. The early departure from elastic behavior prior to the plateau is much less pronounced. The change in the void shape begins just at the point the mean stress deviates from elastic behavior: Q_{20} goes rapidly from the positive value acquired during elastic expansion to a negative value, *i.e.*, from a prolate shape (elongated in the direction of the strain) to an oblate shape (expanded in the transverse directions). Q_2, on the other hand, drops from a positive value, almost reaching zero at the prolate-to-oblate transition point ($\varepsilon = 5.45\%$) and rising even larger value after that [in fact, the oblate shape is somewhat more pronounced than the earlier prolate shape, seen as a larger absolute value of Q_{20} in Fig. 10(a)]. When Q_2 starts to drop Q_4 starts to rise. Then after the prolate-to-oblate transition point, Q_4 begins to saturate. At a strain of $\varepsilon = 5.55\%$, Q_2 is 1.5 times as large as its value at the end of the elastic phase ($\varepsilon = 5.25\%$). Mean plastic strain, equivalent plastic strain, plastic work, and temperature increase together with porosity. Their increase starts immediately at the yield point, *i.e.*, when the mean stress first deviates from the elastic behavior. A bit later than the plastic strain, equivalent plastic strain, plastic work, and temperature, the stress triaxiality increases simultaneously with the first substantial drop in the Mises stress. The fact that the increase in stress-triaxiality follows later is dependent on how the ratio between mean stress and Mises stress develops, as discussed earlier. In Fig. 3(a) and in the data reported in Table I the stress-triaxiality started to increase simultaneously with the mean and Mises stresses deviating from the elastic behavior. The increase of stress-triaxiality is caused by Mises stress plummeting in contrast to nearly constant mean stress. The drop in the Mises stress follows from the flow of dislocations nucleated at the void and from the relaxation of the shear stress of the system due to the flow.

The third region is when the void fraction, mean plastic strain, equivalent plastic strain, plastic work, and temperature switch from rapid increase to a linear growth or even saturate. Subsequently the increase of the stress-triaxiality slows down and plateaus. The value at the plateau is related in continuum models to the ratio of the mean stress threshold for void growth to the flow stress. At the plateau the Mises stress saturates at a small value, close to the tensile strength, and the shape of the void starts to become more of octahedral shape although having a non-zero quadrupole moment, too. Hence at the second and third regions the mean stress is nearly constant, but Mises stress and the stress-triaxiality changes.

A conclusion might be that once the threshold for void growth is reached, the population of dislocations rises sufficiently to relax the shear stress quite effectively and it drops to a low value (the flow stress); the mean stress, on the other hand, plateaus since it is relaxed by void growth and requires that the stress at the void surface be sufficiently high to continue to nucleate dislocations. The fourth region is the failure, when the system breaks, and it is not studied here.

In order to see if the rapid changes studied above are due to the smallness of the size of the void we have done one additional simulation with a system in which the initial void radius is half that in the other simulations; otherwise, the system size is the same, see Fig. 11(b). For the small void simulation, uniaxial strain at a strain-rate $\dot{\varepsilon} = 10^8$/sec has been used. Here the difference is that the quadrupole moment suffers stronger fluctuation due to the smallness of the void, where each of the surface atom contribute more to its value and therefore is even more

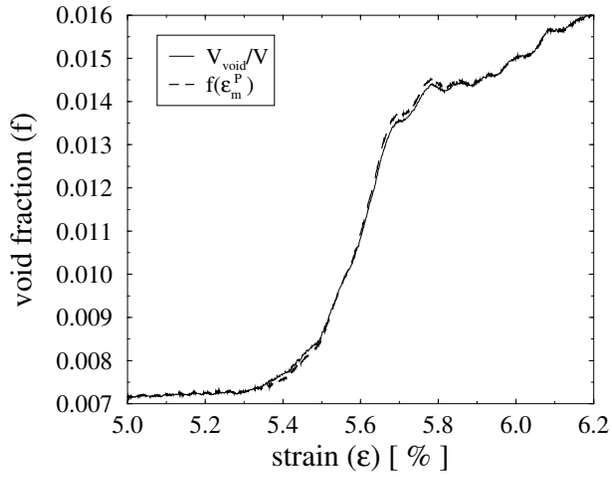

FIG. 12: Porosity f calculated from the actual void fraction as in Eq. (19) with $\delta r = 0.58\, a_0$ (see the text for details of δr) and from the mean plastic strain ε_m^P as in Eq. (25) from the simulation with uniaxial expansion at $\dot{\varepsilon} = 10^8$/sec. See the captions of Figs. 1, 4, 8, and 11 for the simulation details.

sensitive to the selection criterion of surface atoms, and also the shape changes are harder to determine based on the Q_{20} behavior. The other main difference is that the growth of the void is linear all the time. Also the changes in stress-triaxiality in fact advances the porosity when saturating, and the mean stress does not fluctuate but drops more rapidly (this can be compared with the case without the void, where the mean stress drops abruptly).

We have also compared the mean plastic strain and the void volume fraction calculations. In continuum solid mechanics, it is assumed that solid materials are plastically incompressible. Any local dilation, as indicated by a change in the mean strain, is attributed either to elastic dilation or to a change in the porosity of the material, where the porosity is equated to the void volume fraction. The porosity f and the mean plastic strain ε_m^P are then related according to the equation[19]

$$\dot{f} = 3(1-f)\,\dot{\varepsilon}_m^P \tag{24}$$

where the dots denote time derivatives. Integration with respect to time, porosity from f_0 to f, and mean plastic strain from zero to ε_m^P, gives

$$f(\varepsilon_m^P) = 1 + (f_0 - 1)\exp\left(-3\varepsilon_m^P\right). \tag{25}$$

where f_0 is the initial porosity. It is interesting to check whether this relationship holds for the MD simulation, where other effects such as excess volume associated with dislocation cores, vacancies or other defects could require corrections. In comparing the porosity inferred from the mean plastic strain and that calculated directly as the void fraction, the agreement is very good. The trends are in excellent agreement, but there is a small discrepancy between the curves, so that the porosity from the mean plastic strain is overestimated. We believe that the discrepancy arises because of the void surface. In calculating the void fraction, we have defined the void surface to pass through the center of the surface atoms. However, the properties of the surface atoms are distinct from the bulk atoms. Therefore, there is some ambiguity in where the surface should be placed, and a small uniform shift δr of the surface radially into the bulk is enough to account for the discrepancy. In Fig. 12 we have plotted the comparison of the porosity from the mean plastic strain, Eq. (25), and from the void fraction, Eq. (19), using a constant radius increase $\delta r = 0.58\, a_0$, where a_0 is the lattice constant for the void volume calculation. The correction for the void size, δr, varies for different strain-rates and slightly for different loading modes, but is always positive and of the order of the lattice constant, a_0. It should be noted, too, that by Taylor expanding Eq. (25) and discarding the higher order terms, it becomes

$$f(\varepsilon_m^P) = f_0 + 3(1-f_0)\varepsilon_m^P, \tag{26}$$

indicating a linear correspondence between f and ε_m^P as long as the void fraction is small.

VII. CONCLUSIONS AND DISCUSSIONS

In this Article void growth in copper has been studied in a high range of strain-rates at the atomistic level. The model has been designed to simulate the growth of a void nucleating from a very weakly bound inclusion during strain-controlled dynamic fracture. In order to see the effect of various modes of expansion and the related stress-triaxiality, three different modes have been applied, namely uniaxial, biaxial, and triaxial. The molecular dynamics method developed here has been shown to be efficient enough to explore the different loading conditions and strain-rates varying over four orders of magnitude. A uniform expansive loading of a system with periodic boundary conditions has been implemented using a well defined scaling matrix method. For the longest calculations, the MD method was parallelized successfully. The macroscopic observables mean stress, Mises stress, stress-triaxiality, mean plastic strain, equivalent plastic strain, plastic work, and temperature have been calculated and compared with the microscopic quantities measured at the atomistic-level, such as the volume of the void and its shape change. A novel, in this context, method to describe the shape changes in the void is employed, namely calculations of the multipole moments of the void based on spherical harmonics in polynomial, not trigonometric, form. When calculating the volume of the void with an unknown shape or defining solid surface for the multipole moment calculation a useful method, namely optimal triangular tessellation, has been introduced. This method has been extended from the usual planar case to non-planar objects such as the surface of the void.

When the different measured quantities are compared with each other during an MD simulation in uniaxial ex-

pansion, it is found that at early stages of plasticity the Mises stress, and thus also stress-triaxiality, plays a more significant role to the void growth and its shape change than expected. On the other hand, most of the macroscopic plastic quantities as mean and equivalent plastic strain as well as plastic work and temperature, seem to be more dependent on the simultaneous saturation of the mean stress. These calculations show a counter-intuitive behavior, observed previously in continuum void growth modeling,[27,51,52] that a prolate-to-oblate transition occurs. When the system starts to yield, the expansion of the void switches from its original elastic extension in the direction of the load to transverse plastic expansion.

The yield stress values for the lowest strain-rates 10^7/sec are in reasonable agreement with the experimentally measured spall strength.[6] The fact that mean plastic strain can be mapped to the growth of the void is consistent with continuum models.[19]

This study leaves many open questions. For instance related to the void growth are the dislocations, which occur when the system yields. Since the FCC crystal studied here is perfect apart from the void, the dislocations form from void's surface. They are also responsible for its growth by carrying material away. Thus the characterization of plasticity surrounding a growing void at the level of dislocations should be investigated, too, especially with respect to the stress-triaxiality. These investigations are underway.[47] Their results are beyond the scope of this Article, other than to mention that the identification of the yield point in this Article does indeed correspond to the point of initial nucleation of dislocations. Another topic that is beyond the scope of this Article and needs further investigation, but is closely related to the studies here, is the quantitative connection between the shear stress, and thus the mode of the loading, and the onset of the void growth and the resulting change in the stress state. Other areas where this study can be extended are different materials including different lattice structures such as body-centered cubic (BCC) lattices; in the uniaxial case other orientations of the lattice as $\langle 110\rangle$ and $\langle 111\rangle$; continuously changing stress-triaxiality in order to create the full yield surface to the stress space similarly as in Gurson type of continuum studies;[16] to include grain boundaries, defects, pre-existing dislocations, several voids, etc.

Acknowledgments

This work was performed under the auspices of the U.S. Dept. of Energy by the University of California, Lawrence Livermore National Laboratory, under contract number W-7405-Eng-48. The authors would like to thank Dr. Richard Becker bringing to our attention Refs. 51 and 52 that find the prolate-oblate transition in continuum modeling.

APPENDIX A: MULTIPOLE MOMENTS

The 24 different polynomial terms of the multipole moments used in this study are listed below.[58]

The polynomial terms when $l = 1$ are the dipole moments and they capture if the object is offset. The dipole moments are:

$$\begin{aligned} Q_{10} &= \tfrac{1}{2}\sqrt{\tfrac{3}{\pi}}\tfrac{1}{\bar{r}^2}\textstyle\int rz\, d\Omega, \\ \mathrm{Re}\ Q_{11} &= -\tfrac{1}{2}\sqrt{\tfrac{3}{2\pi}}\tfrac{1}{\bar{r}^2}\textstyle\int rx\, d\Omega, \\ \mathrm{Im}\ Q_{11} &= -\tfrac{1}{2}\sqrt{\tfrac{3}{2\pi}}\tfrac{1}{\bar{r}^2}\textstyle\int ry\, d\Omega, \end{aligned} \tag{A1}$$

where $\bar{r}^2 = \frac{1}{4\pi}\int r^2(\theta,\phi)d\Omega$.

Terms with $l = 2$ are the quadrupole moments and they get non-zero values if there is ellipsoidal shape in the object. The quadrupole moments are as follows:

$$\begin{aligned} Q_{20} &= \tfrac{1}{4}\sqrt{\tfrac{5}{\pi}}\tfrac{1}{\bar{r}^2}\textstyle\int 3z^2 - r^2\, d\Omega, \\ \mathrm{Re}\ Q_{21} &= -\tfrac{1}{2}\sqrt{\tfrac{15}{2\pi}}\tfrac{1}{\bar{r}^2}\textstyle\int xz\, d\Omega, \\ \mathrm{Im}\ Q_{21} &= -\tfrac{1}{2}\sqrt{\tfrac{15}{2\pi}}\tfrac{1}{\bar{r}^2}\textstyle\int yz\, d\Omega, \\ \mathrm{Re}\ Q_{22} &= \tfrac{1}{4}\sqrt{\tfrac{15}{2\pi}}\tfrac{1}{\bar{r}^2}\textstyle\int x^2 - y^2\, d\Omega, \\ \mathrm{Im}\ Q_{22} &= \tfrac{1}{2}\sqrt{\tfrac{15}{2\pi}}\tfrac{1}{\bar{r}^2}\textstyle\int xy\, d\Omega. \end{aligned} \tag{A2}$$

Terms with $l = 3$ are the octupole moments and they get non-zero values for tetrahedron shapes:

$$\begin{aligned} Q_{30} &= \tfrac{1}{4}\sqrt{\tfrac{7}{\pi}}\tfrac{1}{\bar{r}^2}\textstyle\int \tfrac{1}{r}z(5z^2 - 3r^2)\, d\Omega, \\ \mathrm{Re}\ Q_{31} &= -\tfrac{1}{8}\sqrt{\tfrac{21}{\pi}}\tfrac{1}{\bar{r}^2}\textstyle\int \tfrac{1}{r}x(5z^2 - r^2)\, d\Omega, \\ \mathrm{Im}\ Q_{31} &= -\tfrac{1}{8}\sqrt{\tfrac{21}{\pi}}\tfrac{1}{\bar{r}^2}\textstyle\int \tfrac{1}{r}y(5z^2 - r^2)\, d\Omega, \\ \mathrm{Re}\ Q_{32} &= \tfrac{1}{4}\sqrt{\tfrac{105}{2\pi}}\tfrac{1}{\bar{r}^2}\textstyle\int \tfrac{1}{r}z(x^2 - y^2)\, d\Omega, \\ \mathrm{Im}\ Q_{32} &= \tfrac{1}{2}\sqrt{\tfrac{105}{2\pi}}\tfrac{1}{\bar{r}^2}\textstyle\int \tfrac{1}{r}xyz\, d\Omega, \\ \mathrm{Re}\ Q_{33} &= -\tfrac{1}{8}\sqrt{\tfrac{35}{\pi}}\tfrac{1}{\bar{r}^2}\textstyle\int \tfrac{1}{r}(x^3 - 3xy^2)\, d\Omega, \\ \mathrm{Im}\ Q_{33} &= \tfrac{1}{8}\sqrt{\tfrac{35}{\pi}}\tfrac{1}{\bar{r}^2}\textstyle\int \tfrac{1}{r}(y^3 - 3x^2y)\, d\Omega. \end{aligned} \tag{A3}$$

And finally the terms with $l = 4$ are listed. They are the hexadecapole moments and capture octahedron shapes:

$$\begin{aligned} Q_{40} &= \tfrac{3}{4}\sqrt{\tfrac{1}{\pi}}\tfrac{1}{\bar{r}^2}\textstyle\int \tfrac{1}{r^2}(3r^4 - 30r^2z^2 + 35z^4)\, d\Omega, \\ \mathrm{Re}\ Q_{41} &= -\tfrac{3}{8}\sqrt{\tfrac{5}{\pi}}\tfrac{1}{\bar{r}^2}\textstyle\int \tfrac{1}{r^2}xz(7z^2 - 3r^2)\, d\Omega, \\ \mathrm{Im}\ Q_{41} &= -\tfrac{3}{8}\sqrt{\tfrac{5}{\pi}}\tfrac{1}{\bar{r}^2}\textstyle\int \tfrac{1}{r^2}yz(7z^2 - 3r^2)\, d\Omega, \\ \mathrm{Re}\ Q_{42} &= \tfrac{3}{8}\sqrt{\tfrac{5}{2\pi}}\tfrac{1}{\bar{r}^2}\textstyle\int \tfrac{1}{r^2}(x^2 - y^2)(7z^2 - r^2)\, d\Omega, \\ \mathrm{Im}\ Q_{42} &= \tfrac{3}{4}\sqrt{\tfrac{5}{2\pi}}\tfrac{1}{\bar{r}^2}\textstyle\int \tfrac{1}{r^2}xy(7z^2 - r^2)\, d\Omega, \\ \mathrm{Re}\ Q_{43} &= -\tfrac{3}{8}\sqrt{\tfrac{35}{\pi}}\tfrac{1}{\bar{r}^2}\textstyle\int \tfrac{1}{r^2}(x^3 - 3xy^2)z\, d\Omega, \\ \mathrm{Im}\ Q_{43} &= -\tfrac{3}{8}\sqrt{\tfrac{35}{\pi}}\tfrac{1}{\bar{r}^2}\textstyle\int \tfrac{1}{r^2}(3x^2y - y^3)z\, d\Omega. \\ \mathrm{Re}\ Q_{44} &= \tfrac{3}{16}\sqrt{\tfrac{35}{2\pi}}\tfrac{1}{\bar{r}^2}\textstyle\int \tfrac{1}{r^2}(x^4 - 6x^2y^2 + y^4)\, d\Omega, \\ \mathrm{Im}\ Q_{44} &= \tfrac{3}{4}\sqrt{\tfrac{35}{2\pi}}\tfrac{1}{\bar{r}^2}\textstyle\int \tfrac{1}{r^2}xy(x^2 - y^2)\, d\Omega. \end{aligned} \tag{A4}$$

[1] See *e.g.*, J. F. Knott, *Fundamentals of Fracture Mechanics*, (Butterworths, London 1973).

[2] See *e.g.*, *High-Pressure Shock Compression of Solids II: Dynamic Fracture and Fragmentation*, edited by L. Davison, D. E. Grady, and M. Shahinpoor, (Springer-Verlag, 1996).

[3] D. R. Curran, L. Seaman, and D. A. Shockey, Phys. Rep. **147**, 253 (1987).

[4] F. A. McClintock in *Metall. Eff. at High Strain Rates*, (Plenum Press, New York, 1973).

[5] T. W. Barbee Jr., L. Seaman, R. Crewdson, and D. Curran, J. of Materials **7**, 393 (1972).

[6] See G. I. Kanel, S. V. Razorenov, and A. V. Utkin in *High-Pressure Shock Compression of Solids II: Dynamic Fracture and Fragmentation* (Ref. 2).

[7] V. Tvergaard and A. Needleman, Acta metall. **32**, 157 (1984).

[8] V. Tvergaard and A. Needleman, Int. J. of Fracture **59**, 53 (1993).

[9] A. Needleman and V. Tvergaard, Eur. J. Mech. A **17**, 421 (1998).

[10] F. A. McClintock, J. Appl. Mech. No. 6, 363 (1968).

[11] J. R. Rice and D. M. Tracey, J. Mech. Phys. Solids **17**, 201 (1969).

[12] R. J. Green, Int. J. Mechanical Science **14**, 215 (1972).

[13] A. Needleman, J. Appl. Mech. **39**, 964 (1972).

[14] L. M. Brown and J. D. Embury in *Proc. 3rd Int. Conf. on Strength of Metals and Alloys*, (Institute of Metals, London, 1973).

[15] S. Shima and M. Oyane, Int. J. Mechanical Science **18**, 285 (1976).

[16] A. L. Gurson, J. Eng. Mater. and Tech. **99**, 2 (1977).

[17] V. Tvergaard, Int. J. of Fracture **17**, 389 (1981).

[18] A. C. F. Cocks and M. F. Ashby, Progress in Materials Science **27**, 189 (1982).

[19] V. Tvergaard, Adv. Appl. Mech. **27**, 83 (1990).

[20] Y. Huang, J. W. Hutchinson, and V. Tvergaard, J. Mech. Phys. Solids **39**, 223 (1991).

[21] R. Cortes, Int. J. Solids Structures **29**, 1339 (1992).

[22] A. Needleman, V. Tvergaard, and E. v. d. Giessen, Int. J. Damage Mech. **4**, 134 (1995).

[23] V. Tvergaard and A. Needleman, Int. J. Solids Structures **32**, 1063 (1995).

[24] E. van der Giessen, M. W. D. van der Burg, A. Needleman, and V. Tvergaard, J. Mech. Phys. Solids **43**, 123 (1995).

[25] J. Y. Shu, Int. J. Plasticity **14**, 1085 (1998).

[26] X. Y. Wu XY, K. T. Ramesh, T. W. Wright, J. Mech. Phys. Solids **51**, 1 (2003); Int. J. Solids Structures **40**, 4461 (2003).

[27] P. Ponte Castañeda and M. Zaidman, J. Mech. Phys. Solids **42**, 1459 (1994), and references therein.

[28] J. Belak, in *Shock Compression of Condensed Matter*, edited by Schmidt *et al.*, (American Institute of Physics, 1997).

[29] J. Belak, J. Comp. Aid. Mat. Design **5**, 193 (1998).

[30] J. Belak and R. Minich in *Mat. Res. Soc. Symp. Proc.* **539** (Materials Research Society, 1999).

[31] R. E. Rudd and J. Belak, Comp. Mat. Science, **24**, 148 (2002).

[32] E. T. Seppälä, J. Belak, and R. E. Rudd, ICES'02 proceedings, (Tech. Science Press, 2002), in press.

[33] E. T. Seppälä, J. Belak, and R. E. Rudd, in *Dislocations, Plasticity and Metal Forming*, edited by Akhtar S. Khan (NEAT Press, Maryland, 2003).

[34] L. Farrisey, M. Ludwig, P. E. McHugh, and S. Schumauder, Comp. Mat. Science **18**, 102 (2000).

[35] M. R. Gungor, D. Maroudas, and S. Zhou, Appl. Phys. Lett., **77**, 343 (2000).

[36] S. J. Zhou, D. M. Beazley, P. S. Lomdahl, and B. L. Holian, Phys. Rev. Lett. **78**, 479 (1997).

[37] F. F. Abraham, R. Walkup, H. J. Gao, M. Duchaineau, T. D. De la Rubia, M. Seager, Proc. Natl. Acad. Sci. USA, **99**, 5783 (2002).

[38] M. P. Allen and D. J. Tildesley, *Computer Simulations of Liquids* (Oxford University Press, 1987).

[39] D. J. Oh and R. A. Johnson, J. Mater. Res. **3**, 471 (1988).

[40] D. J. Oh and R. A. Johnson, in *Atomistic Simulation of Materials: Beyond Pair Potentials*, edited by V. Vitek and D. Srolovitz, (Plenum, New York, 1989).

[41] W. G. Hoover, Phys. Rev. A **31**, 1695 (1985).

[42] M. Parrinello and A. Rahman, J. Appl. Phys. **52**, 7182 (1981).

[43] See *e.g.* G. E. Dieter, *Mechanical Metallurgy*, (McGraw-Hill, Boston, 1986).

[44] See *e.g. Engineering Materials: Properties and Selection, 6th ed.*, p. 532, edited by K. G. Budinski and M. K. Budinski, (Prentice Hall, Upper Saddle River, NJ, 1999).

[45] J. D. Eshelby, Proc. Royal Soc. A **241**, 376 (1957).

[46] N. W. Aschroft and N. D. Mermin, *Solid State Physics*, (Saunders College Press, 1976).

[47] E. T. Seppälä, J. Belak, and R. E. Rudd, unpublished.

[48] See *e.g.* R. Hill, *The Mathematical Theory of Plasticity*, (Clarendon Press, Oxford, 1950).

[49] S. W. Sloan, Comput. Struct. **47**, 441 (1993).

[50] E. T. Seppälä, J. Belak, and R. E. Rudd, unpublished.

[51] B. Budiansky, J. W. Hutchinson, and S. Slutsky in *Mechanics of Solids. The Rodney Hill Anniversary Volume*, edited by. H. G. Hopkins and M. J. Sewell, (Pergamon Press, Oxford, 1982).

[52] H. Andersson, J. Mech. Phys. Solids **25**, 217 (1977).

[53] M. Gologanu, J.-P. Leblond, and J. Devaux, J. Mech. Phys. Solids **41**, 1723 (1993).

[54] M. Gologanu, J.-P. Leblond, and J. Devaux, J. Eng. Mater. and Tech. **116**, 290 (1994).

[55] A. L. Stevens, L. Davison and W. E. Warren, J. Appl. Phys. **43**, 4922 (1972).

[56] D. J. Eaglesham, A. E. White, L. C. Feldman, N. Moriya, and D. C. Jacobson, Phys. Rev. Lett. **70**, 1643 (1993).

[57] See *e.g.* J. D. Jackson, *Classical Electrodynamics*, (John Wiley & Sons, New York, 1975).

[58] See *e.g.* A. J. Stone, *The Theory of Intermolecular Forces* (Clarendon Press, Oxford, 1996), Appendix E.

[59] P. J. Steinhardt, D. R. Nelson, and M. Ronchetti, Phys. Rev. B **28**, 784 (1983).

[60] *CRC Standard Mathematical Tables*, p. 146 edited by W. H. Beyer, (CRC Press, Boca Raton, 1984, 27th edition).